OXFORD

ORIGINAL ARTICLE

Immune dysregulation may contribute to disease pathogenesis in spinal muscular atrophy mice

Marc-Olivier Deguise[1,2,3], Yves De Repentigny[1,3], Emily McFall[1,3], Nicole Auclair[1,4], Subash Sad[5] and Rashmi Kothary[1,2,3,6,*]

[1]Regenerative Medicine Program, Ottawa Hospital Research Institute, Ottawa, Ontario, Canada K1H 8L6, [2]Department of Cellular and Molecular Medicine, [3]Centre for Neuromuscular Disease, University of Ottawa, [4]Faculty of Science, University of Ottawa, Ottawa, Ontario, Canada, K1N 9B4, [5]Department of Biochemistry, Microbiology, and Immunology and [6]Department of Medicine, University of Ottawa, Ottawa, Ontario, Canada K1H 8M5

*To whom correspondence should be addressed at: Rashmi Kothary, Ottawa Hospital Research Institute, 501 Smyth Road, Ottawa, Ontario, Canada K1H 8L6. Tel: +613 7378707; Fax: +613 7378803; Email: rkothary@ohri.ca

Abstract

Spinal muscular atrophy (SMA) has long been solely considered a neurodegenerative disorder. However, recent work has highlighted defects in many other cell types that could contribute to disease aetiology. Interestingly, the immune system has never been extensively studied in SMA. Defects in lymphoid organs could exacerbate disease progression by neuroinflammation or immunodeficiency. Smn depletion led to severe alterations in the thymus and spleen of two different mouse models of SMA. The spleen from Smn depleted mice was dramatically smaller at a very young age and its histological architecture was marked by mislocalization of immune cells in the $Smn^{2B/-}$ model mice. In comparison, the thymus was relatively spared in gross morphology but showed many histological alterations including cortex thinning in both mouse models at symptomatic ages. Thymocyte development was also impaired as evidenced by abnormal population frequencies in the $Smn^{2B/-}$ thymus. Cytokine profiling revealed major changes in different tissues of both mouse models. Consistent with our observations, we found that survival motor neuron (Smn) protein levels were relatively high in lymphoid organs compared to skeletal muscle and spinal cord during postnatal development in wild type mice. Genetic introduction of one copy of the human SMN2 transgene was enough to rescue splenic and thymic defects in $Smn^{2B/-}$ mice. Thus, Smn is required for the normal development of lymphoid organs, and altered immune function may contribute to SMA disease pathogenesis.

Introduction

Spinal muscular atrophy (SMA) is an inherited fatal neurological disease characterized by alpha motor neuron loss and neurogenic atrophy. The disease-causing gene is Survival Motor Neuron 1 (*SMN1*), which codes for a ubiquitously expressed protein (1–3). After close to 20 years of innovative research, a cure or treatment is still is not available to patients. In fact, although motor neurons are primary targets in SMA, the specific aetiology of disease pathogenesis remains uncertain. It is still unknown why motor neurons are particularly susceptible to

depletion of the ubiquitously expressed SMN protein in comparison to other organs or cell types. As a result, the SMA field continues to debate whether or not SMA should be considered a motor neuron disease or a multi-organ disease (4–6).

Consequently, pre-clinical therapeutic endeavours aim at increasing levels of SMN through various approaches - either solely in the nervous system or systemically. Importantly, systemic delivery of antisense oligonucleotides (ASOs) to increase SMN levels results in a better outcome than administration solely in the central nervous system (7). Moreover, delivery of ASOs only in the periphery was sufficient to increase lifespan and improved motor functions in a mouse model of SMA (8). Such evidence highlights the importance of other cell types in SMA pathogenesis. This is consistent with studies showing that other cell types are also affected in SMA, albeit to a lesser extent than the motor neurons. Examples include cell types that have a close relationship with motor neurons, such as skeletal muscles and astrocytes, to cell types that are completely unrelated, such as the gastrointestinal system, heart, pancreas and liver (9–25). Astrocytes of $Smn\Delta7$ ($Smn^{-/-};SMN2^{+/+};Smn^{\Delta7/\Delta7}$) model mice and SMA human iPSC-derived astrocytes show many signs of activation, with the latter also showing impaired calcium handling (9). Moreover, the restoration of SMN uniquely in these cells significantly increases lifespan, weight, and motor functions in two mouse models of SMA (10). Similarly, several studies have shown intrinsic defects in skeletal muscles. SMA model mice have a delay in muscle growth highlighted by dysregulation of important myogenic transcription factors (13,16). Consequently, differentiation and fusion of myoblasts is impaired (11–13,16). Likewise, the hearts of SMA model mice display changes in functions on multiple levels. They are bradycardic, smaller and have a decreased ejection fraction indicative of possible cardiac insufficiency (17–20). Recently, elevation of the E3 ligase atrogin-1 and autophagy markers have been reported in the hearts of severe $Smn^{-/-};SMN2$ ($Smn^{-/-};SMN2^{+/+}$) mice at symptomatic age, revealing potential intrinsic molecular underpinnings of these defects (15). Clinically, some patients with the more severe presentation of SMA also have co-existing heart conditions (26,27). Metabolically, both patients and mouse models have abnormal lipid and glucose profiles compared to controls (21,22,28,29). Therefore, collectively it seems likely that SMA is the cumulative result of defects in multiple cell types.

The immune system has not been studied in the context of SMA. Yet, it is possible that immune dysregulation could make SMA patients more prone to infection or exacerbate their current disease state. The immune system is divided into two major branches, the innate and adaptive responses, which are each controlled by different populations of immune cells (30,31). The adaptive (or acquired) immune response is mediated mainly by lymphocytes such as T-cells and B-cells (30,31). These cells develop in primary lymphoid organs, such as the bone marrow and the thymus. Unlike the B-cells, which exclusively develop in the bone marrow, the thymus is essential in T-cell development and maturation (30,31). Fully mature B-cells and T-cells will migrate in the periphery and most will reside in secondary lymphoid organs such as the lymph nodes and the spleen (30,31). The spleen is involved in a wider array of processes including blood filtration, hematopoiesis, iron metabolism and fighting infection, especially of encapsulated bacteria (32,33). In the context of SMA, there has been one brief report indicating smaller thymus and spleen in the $Smn^{-/-};SMN2$ severe mouse model, likely due to increased apoptosis (34).

Here, we have characterized the gross morphology and basic tissue architecture of the spleen and thymus in both $Smn^{-/-};SMN2$ and $Smn^{2B/-}$ model mice. We further examined lymphocyte development in the thymus. Finally, we performed cytokine profiling in these organs and in the serum to understand any functional impairment. Altogether, we report important changes in both the spleen and thymus of two SMA model mice, which appear to initiate in secondary lymphoid organs. Overall, our work demonstrates that immune dysregulation is likely contributing to the overall clinical picture of SMA.

Results

The spleen is decreased in size in two mouse models of SMA

Based on initial observations during dissection, a thorough temporal examination of the abnormal gross morphology of the spleen in $Smn^{2B/-}$ and $Smn^{-/-};SMN2$ mice was performed. Different strategies of normalization (spleen length/mouse weight, spleen length/tibia length, spleen length/mouse length, spleen length/brain weight) all yielded similar results (Supplementary Material, Fig. S1A–D). Moreover, spleens from both male and female $Smn^{2B/-}$ mice showed similar results (Supplementary Material, Fig. 1). Therefore, the data were normalized to mouse length and weight, and included both genders. The spleen gross morphology in $Smn^{2B/-}$ mice was compared to control littermates at various ages to better appreciate the progression of events. At postnatal day 0 (P0), changes to the size of spleens of $Smn^{2B/-}$ mice were not observed (Fig. 1A–C). Significant reductions were observed in both spleen weight/body weight and spleen length/total body length ratios at P19 (Fig. 1M–O), P14 (Fig. 1J–L), P9 (Fig. 1G–I), and P4 (Fig. 1D–F) in the $Smn^{2B/-}$ mice, albeit of diminishing severity at younger ages. Overall, the progression of changes in spleen size followed an inverse function with time (Fig. 1P). $Smn^{2B/-}$ spleens often appeared necrotic, likely due to splenic infarct. Quantification showed that spleens from P19 $Smn^{2B/-}$ mice are 2.26 times more likely to have an infarction compared to wild type but not $Smn^{2B/+}$ mice (Supplementary Material, Fig. S2). The infarct size was not graded, but there did not appear to be any appreciable difference based on qualitative assessment. To better understand the underlying pathology of living immune cells, necrotic spleens were not included in subsequent analysis.

Examination of spleens from the severe $Smn^{-/-};SMN2$ mice at P5 revealed a clear difference in both weight and length of the spleen compared to wild type and heterozygous mice (Fig. 2G–I), similar to previous reports (34). In addition, significant changes in both weight and length of the spleen were observed at P2 (Fig. 2D–F). Changes in spleen size were not observed at birth (P0) (Fig. 2A–C). Overall, the changes in size of $Smn^{-/-};SMN2$ spleens become progressively worse over time (Fig. 2J). Altogether, the spleens of SMA model mice are significantly smaller than those from control mice, and this defect is present before any overt motor neuron pathology (35,36).

Architectural disorganization in the spleen is more prominent in the less severe Smn²ᴮ/⁻ mice than in the severe Smn⁻/⁻;SMN2 mice

The spleen histology is highly sophisticated with different regions harbouring different functions. The red pulp is a region where incoming blood from arteries is filtered (32). The white
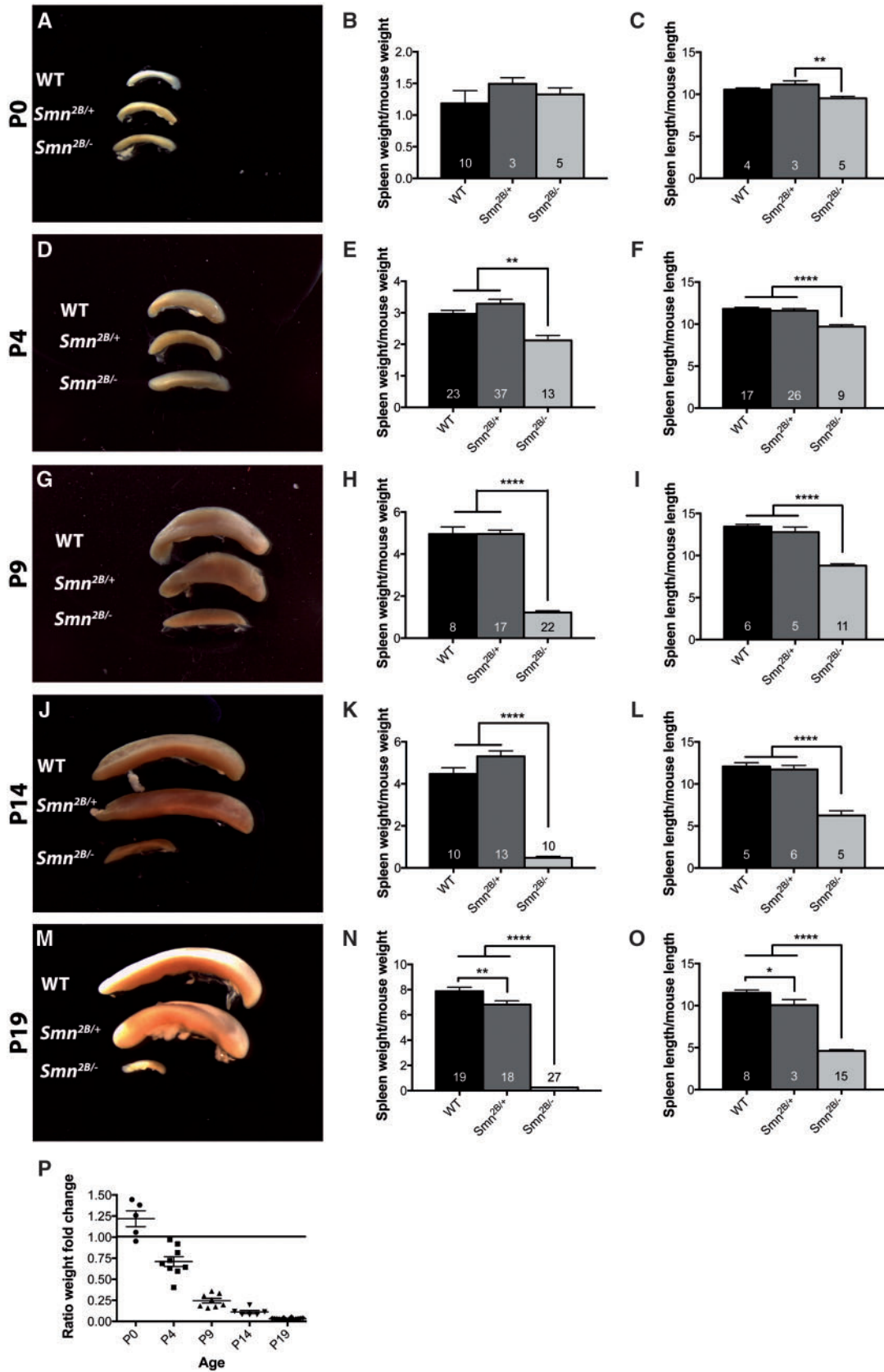
Figure 1. $Smn^{2B/-}$ mice have significantly smaller spleens beginning at a young age. Representative images and quantification of the weight and length ratios of the spleens from wild type, $Smn^{2B/+}$, and $Smn^{2B/-}$ mice at P0 (**A-C**), P4 (**D-F**), P9 (**G-I**), P14 (**J-L**), P19 (**M-O**). (**P**) Spleen size is inversely correlated with age. (The n value for each experiment is as written in the graph bars, one-way ANOVA with bonferroni post-test. $P \leq 0.05$ for *, $P \leq 0.01$ for **, $P \leq 0.001$ for *** and $P \leq 0.0001$ for ****).
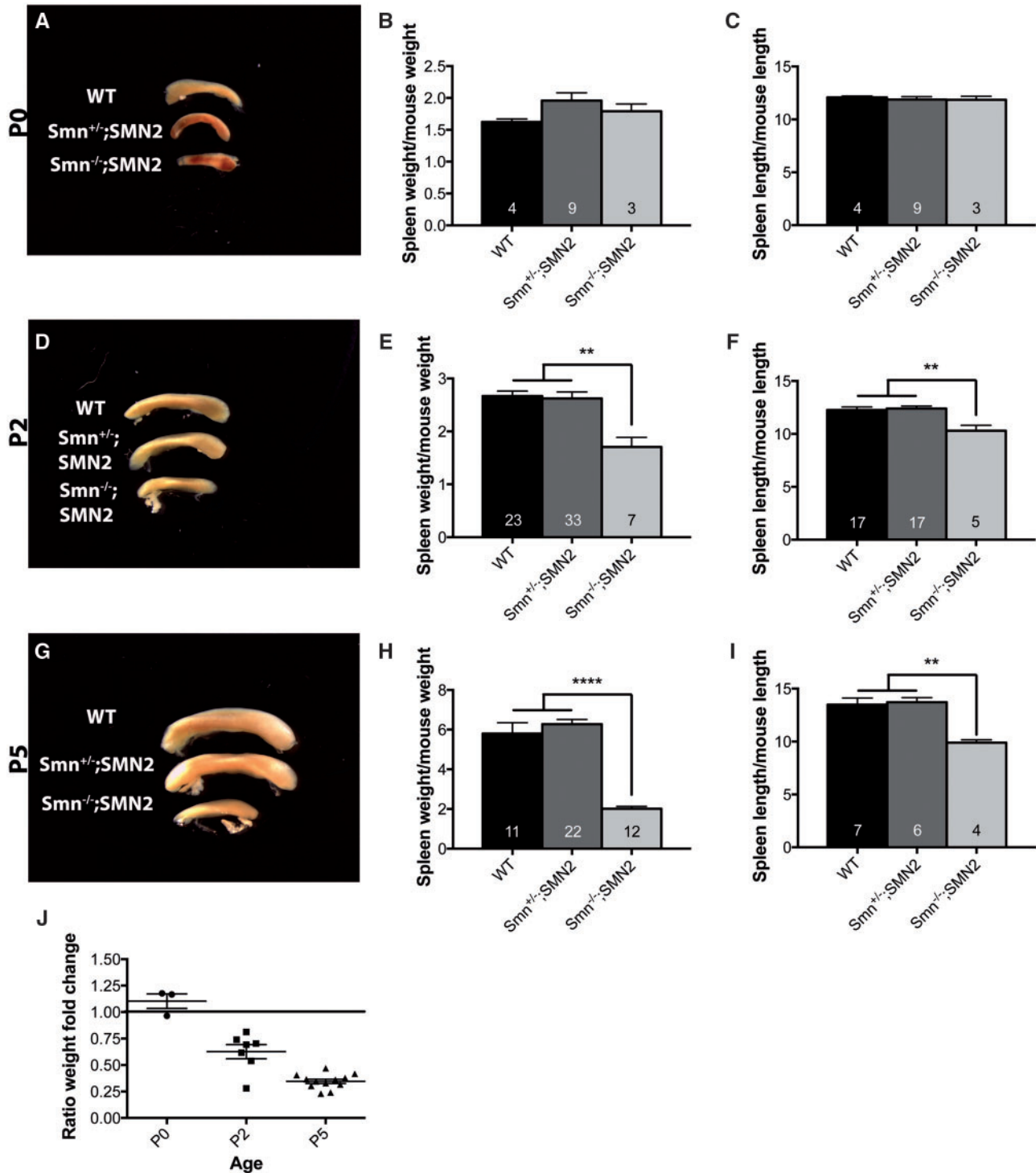
Figure 2. $Smn^{-/-};SMN2$ mice also have smaller spleens from a young age. Representative images and quantification of the weight and length ratios of the spleens from wild type, $Smn^{+/-};SMN2$, and $Smn^{-/-};SMN2$ mice at P0 (**A-C**), P2 (**D-F**), P5 (**G-I**). (**J**) Spleen size is inversely correlated with age. (The n value for each experiment are as written in the graph bars, one-way ANOVA with bonferroni post-test, $P \leq 0.05$ for *, $P \leq 0.01$ for **, and $P \leq 0.0001$ for ****).

pulp contains mostly lymphoid cells such as B-cells and T-cells, which are segregated into two compartments of their own (32). The T-cells are present around the arteriole (often denoted as the periarteriolar lymphoid sheath - PALS) while the B-cells are distributed in follicles within the PALS (32). The red pulp and white pulp are separated by a marginal zone composed mainly

of macrophages and marginal zone B-cells (32). Macrophages can also be found diffusely in the red pulp where they play an important role in iron metabolism (32). Hematoxylin and eosin (H&E) staining was performed on spleen sections at P0, P4, P9, P14 and P19 for the $Smn^{2B/-}$ mice and at P2 and P5 for the $Smn^{-/-};SMN2$ mice (Fig. 3). The architecture of the spleen from
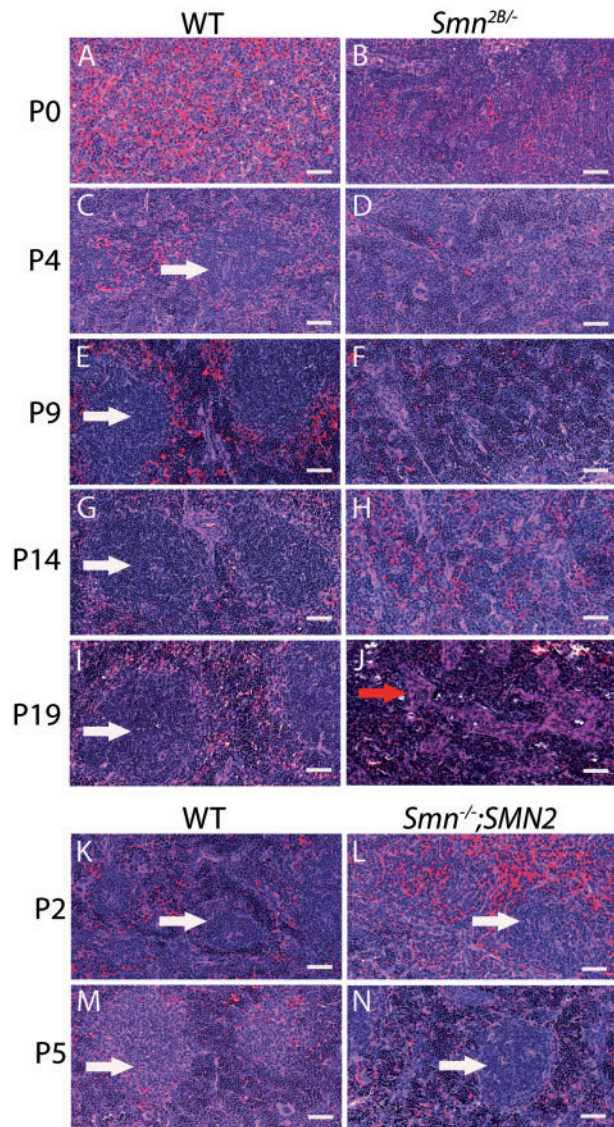
Figure 3. Abnormal spleen architecture in $Smn^{2B/-}$ mice but not in $Smn^{-/-};SMN2$ mice. Representative 40X images of sections of spleen after H&E staining of wild type and $Smn^{2B/-}$ mice at P0 (**A,B**), P4 (**C,D**), P9 (**E,F**), P14 (**G,H**), and P19 (**I,J**). Disruption of white pulp formation is apparent already at P4 in the spleens of $Smn^{2B/-}$ mice. Accumulation of smooth muscle cells is apparent at P19 (**J**). Representative images of sections of spleen after H&E staining of wild type and $Smn^{-/-};SMN2$ mice at P2 (**K,L**) and P5 (**M,N**). White pulp was readily identifiable (white arrows). The red arrow identifies area of smooth muscle cell accumulation. Scale bar represent 50 μm. (n = 3 for all samples except for P0 $Smn^{2B/-}$ mice, where n = 2 and P2, P5 $Smn^{-/-};SMN2$ mice, where n = 4).

$Smn^{2B/-}$ mice was clearly disrupted with effacement of the clear margin of the white pulp at P19 in comparison to wild type mice (Fig. 3I and J). Additionally, all $Smn^{2B/-}$ spleens analysed appeared hyperchromatic with accumulation of fibrotic-like tissue and smooth muscle cells (Fig. 3J). This is possibly due to necrosis or apoptosis, which could explain their small size. Indeed, spleen stained for smooth muscle actin revealed altered localization with increased clumping of smooth muscle cells in contrast to wild type spleens at P19 (Supplementary Material, Fig. S3). When analysing earlier time points, namely P14, P9 and P4 (Fig. 3C–H), a similar characteristic loss of

white pulp borders was observed. We primarily observed red pulp and no white pulp at P0 for both wild type and $Smn^{2B/-}$ mice (Fig. 3A and B), consistent with previous studies (37). Remarkably, the $Smn^{-/-};SMN2$ model mice did not have a disruption of the red and white pulp architecture at P2 or at P5 (Fig. 3M and N).

Immune cells in the spleen are mislocalized in the $Smn^{2B/-}$ mice but not in the severe $Smn^{-/-};SMN2$ mice

To better characterize the changes in architecture in the spleens of $Smn^{2B/-}$ and $Smn^{-/-};SMN2$ mice, immunohistochemistry was performed to label T-cells, B-cells, and macrophages (Fig. 4). The analysis of P4 $Smn^{2B/-}$ spleens clarified that white pulp are potentially still forming at this age in the mutant mice as shown by staining of the T-cell marker CD3 around blood vessels (Fig. 4B and F). This reflects the positioning of the T-cells in the PALS. However, the B-cell marker CD19 and the macrophage marker F4/80 staining was diffuse in P4 $Smn^{2B/-}$ spleen and did not surround the PALS as in wild type (Fig. 4C,G and D,H respectively). This could indicate possible infiltration of both B-cells and macrophages into what should be the white pulp. At P19, staining of CD3, CD19 and F4/80 revealed a severe mislocalization of T-cells, B-cells and macrophages in $Smn^{2B/-}$ spleens compared to control (Fig. 4B'H'). Unlike wild type, T-cell marker CD3 staining (Fig. 4B',F') in $Smn^{2B/-}$ spleens showed very diffuse distribution with no clear white pulp conformation and PALS region, confirming the results from the H&E staining (Fig. 4A',E'). Similarly, B-cell marker CD19 and macrophage marker F4/80 staining did not show the marginal zone pattern in $Smn^{2B/-}$ spleen in comparison to wild type (Fig. 4C',G' and D',H', respectively). However, some unclear oval-shaped regions with decreased density of CD19 staining were present in $Smn^{2B/-}$ mice (Fig. 4G'). These might be attributed to the accumulation of smooth muscle identified on H&E staining and immunostaining since similar low density areas were observed in CD3 stained spleens (Fig. 4F'). Strikingly, the immunostaining assessment in the spleens from $Smn^{-/-};SMN2$ mice revealed that the structures were largely unaffected, similar to the results obtained from the H&E staining (Fig. 4I-P and I'-P'). The difference between the two SMA mouse models at symptomatic ages is quite interesting. Such differences between models have previously been reported in other contexts in SMA and it is possible that such changes require time and/or other factors to present themselves (13,15). Altogether, these results suggest a defective segregation of the white and red pulp in $Smn^{2B/-}$ spleens. Remarkably, the localization of these various immune cells confirms that the white pulp may be absent in the spleens of $Smn^{2B/-}$ mice, which could impair fundamental splenic functions. However, the progression of events leading to what appears to be a loss of white pulp formation remains to be determined.

The thymus is decreased in size in symptomatic $Smn^{2B/-}$ mice but not in $Smn^{-/-};SMN2$ mice

Our comparison of the various organs showed a trend towards a decrease in the ratio of the thymus weight over mouse weight in $Smn^{2B/-}$ mice at P19 (Supplementary Material, Fig. 4). An examination of the thymus at P4 and P19 showed that it was significantly smaller at P19 but not at P4 in $Smn^{2B/-}$ mice compared to $Smn^{2B/+}$ and wild type controls (Fig. 5A–D). We next compared these gross morphological changes in the spleen and
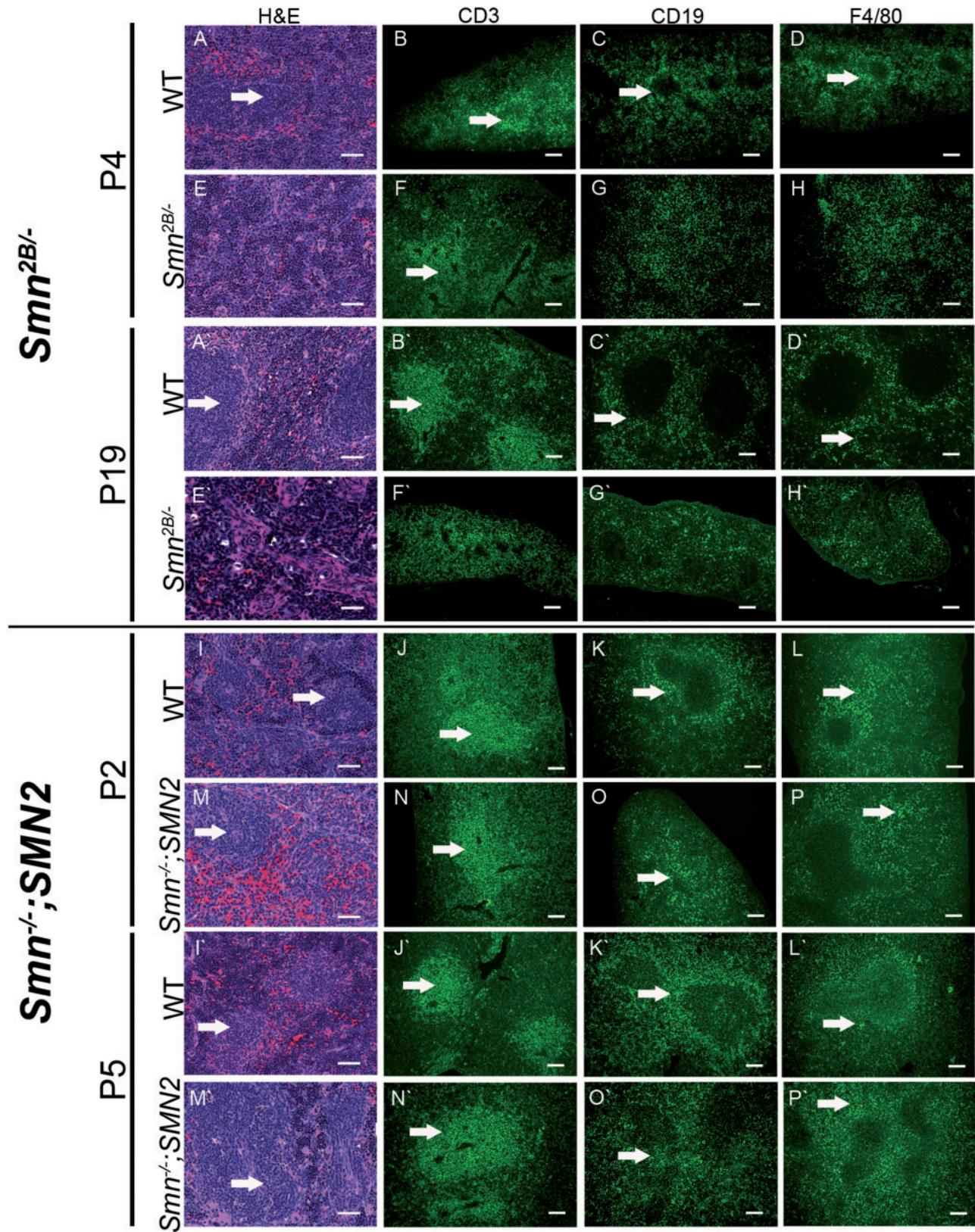
Figure 4. T-cells, B-cells and macrophages are mislocalized in the spleens of symptomatic *Smn*[2B/-] mice but not of *Smn*^{-/-};SMN2 mice. Representative images of H&E, CD3, CD19, and F4/80 staining of wild type and *Smn*[2B/-] spleen sections at P4 (**A-H**) and P19 (**A'-H'**). The T-cell marker CD3 staining was present in the PALS at P4 but was very diffuse at P19 in the *Smn*[2B/-] samples. The staining patterns of the B-cell marker CD19 and the macrophage marker F4/80 were diffuse at P4 and P19. Representative images of H&E, CD3, CD19, and F4/80 staining of wild type and *Smn*^{-/-};SMN2 spleen sections at P2 (**I-P**) and P5 (**I'-P'**). No mislocalization of immune cells at either time points was apparent in this mouse model. The white arrows identify areas where staining was expected. Scale bar represent 50 μm for H&E images and 20 μm for immunostaining images. (n = 4 at P4, n = 4 at P19, n = 2 at P2, n = 2 at P5).
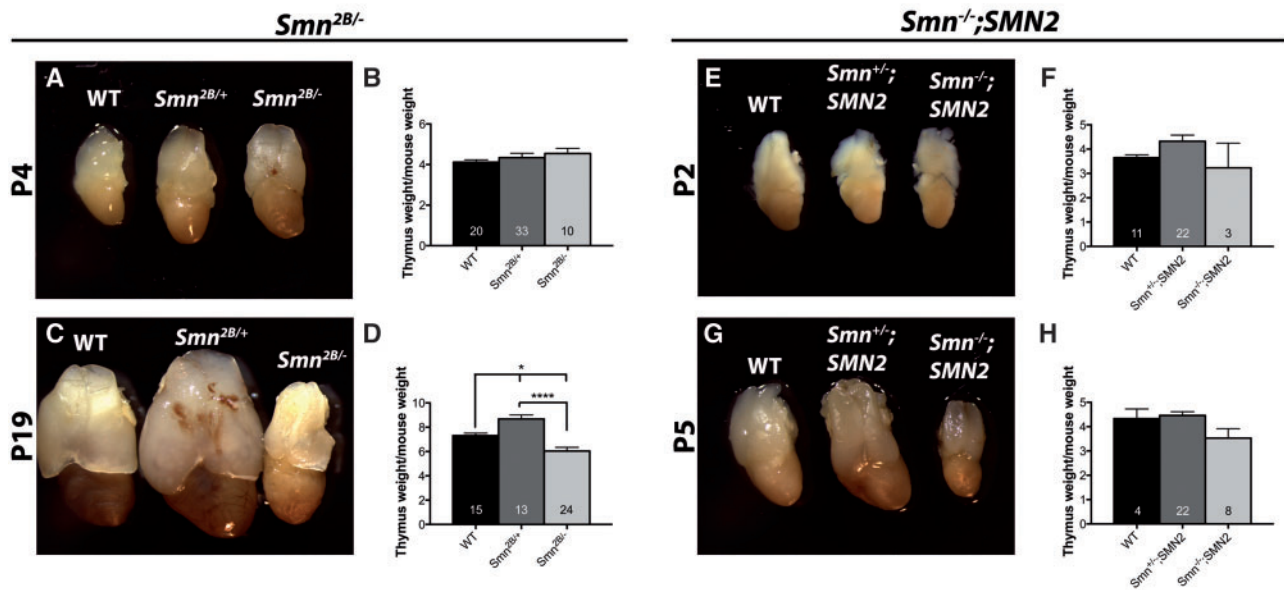
Figure 5. The thymus is smaller in symptomatic $Smn^{2B/-}$ mice but not in $Smn^{-/-};SMN2$ mice. Representative images and quantification of the thymus weight to mouse weight ratios from $Smn^{2B/-}$ mice at P4 (**A,B**) and P19 (**C,D**), and from $Smn^{-/-};SMN2$ mice at P2 (**E,F**) and P5 (**G,H**). (The n value for each experiment are as written in the graph bars, one-way ANOVA with bonferroni post-test, $P \le 0.05$ for *, and $P \le 0.0001$ for ****).

thymus to other organs such as the liver and kidneys of some of the same animals. We did not observe similar decreases in relative size at P4 or P19 for liver and kidney (Supplementary Material, Fig. 4A and B), suggesting that the reduction in size is specific to lymphoid organs. Previous findings had indicated that $Smn^{-/-};SMN2$ mice had smaller thymus at P5 (34). Interestingly, we did not observe a decrease in thymus size in the $Smn^{-/-};SMN2$ mice at any stage (Fig. 5E–H), although there was a trend toward smaller thymus size at P5.

Architectural defects are also present in thymus of symptomatic Smn$^{2B/-}$ mice

The thymus is normally composed of the cortex (outer zone), where early development of T-cells occur (double negative - DN - CD4^{-ve}; CD8^{-ve} and double positive - DP - CD4$^+$; CD8$^+$), and the medulla (inner zone), where final maturation of CD4$^+$ (CD4 single positive - SP) or CD8$^+$ (CD8 single positive - SP) cells occurs (38). At P19, striking abnormalities in sections of thymus from $Smn^{2B/-}$ mice were apparent. There was a clear reduction in cellularity and cortex thinning compared to wild type controls (Fig. 6G–L). An increase in the number of apoptotic bodies and tingible body macrophages was evident by the classical 'starry-sky' appearance in the majority of the animals analysed (Fig. 6H and K) (39). The comparison of cross-sectional area of the lobe of the thymus confirmed the decreased size observed in morphological assessments (Fig. 6I). We next assessed whether such changes were also present in the thymus at P4, a time when we first observed spleen abnormalities. Interestingly, no significant changes were present at this age (Fig. 6A–F).

We next performed the same analysis on the thymus from the $Smn^{-/-};SMN2$ mice. The H&E staining of the $Smn^{-/-};SMN2$ thymus revealed a very similar pathology at the late stage (P5) but not at a early stage (P2), as we observed in the $Smn^{2B/-}$ thymus (Supplementary Material, Fig. S5). However, these changes were of lesser severity, likely due to the shortened lifespan of the $Smn^{-/-};SMN2$ mice.

To follow up on our observations on the apoptotic bodies in the thymus of $Smn^{2B/-}$ mice, a more thorough analysis was performed. TUNEL and cleaved caspase 3 staining revealed increased positive punctae in P19 $Smn^{2B/-}$ thymus in comparison to wild type (Supplementary Material, Fig. S6A–F). Analysis of several pro-apoptotic (Bax, Caspase 2 (Casp2), Caspase 8 (Casp8), Fas receptor (FasR) and p53), anti-apoptotic (Bcl2), and autophagy markers (Bnip3, Gabarapl1 and CathepsinL) revealed a general trend in increase in transcript levels in both pro-apoptotic and autophagy genes at P19 but did not reach significance, implying that cell death might have already occurred (Supplementary Material, Fig. S6H). At P4, a time where no pathology is observed in the $Smn^{2B/-}$ thymus, transcript expression levels were relatively unchanged with the exception of p53 (Supplementary Material, Fig. S6G). Interestingly, a similar profile was present in P5 $Smn^{-/-};SMN2$ thymus with the increase in the mRNA levels of several markers being statistically significant (Supplementary Material, Fig. S6J). Once again, at the earlier time point (P2), little change was observed in the $Smn^{-/-};SMN2$ thymus (Supplementary Material, Fig. S6J).

T-cell development is misregulated only in symptomatic Smn$^{2B/-}$ mice

The spleen gross morphological changes in the SMA model mice may be a consequence of abnormal immune cell development given that both $Smn^{2B/-}$ and $Smn^{-/-};SMN2$ mouse models show thymic architectural abnormalities. Specifically, the progenitor cell may not get into the thymus as efficiently or get stalled in the thymus at any point in development, which would lead to fewer cells migrating to the spleen and therefore partly explaining its small size. We therefore decided to perform a systematic assessment of T-cell development in $Smn^{2B/-}$ mice. T-cell development is a complex multi-step process in which cells are passaged through different organs before becoming fully functional. First, hematopoietic cells migrate from the bone marrow to the thymus, where they commit to the T-cell lineage
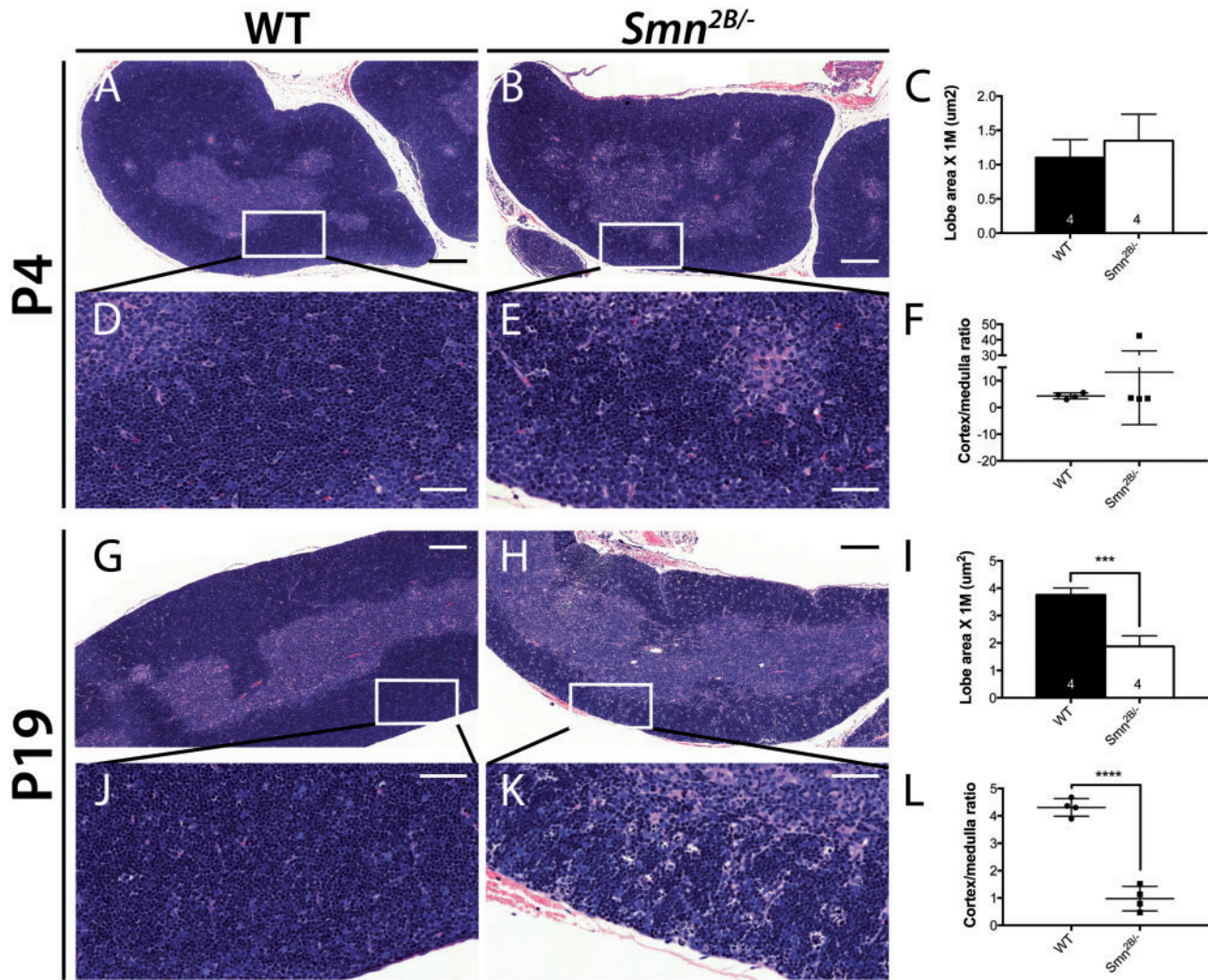
Figure 6. Abnormal thymic architecture in symptomatic $Smn^{2B/-}$ mice. Representative 10X images of H&E stained sections of thymus showing the medulla and cortex in wild type and $Smn^{2B/-}$ mice at P4 (**A,B**) and P19 (**G,H**). Representative 50X images of the cortex in the thymus of wild type and $Smn^{2B/-}$ mice at P4 (**D,E**) and P19 (**J,K**). Quantification of the average thymic lobe area (**C**) and cortex/medullary area ratio (**F**) showed no difference between $Smn^{2B/-}$ and wild type mice at P4. Quantification of the average thymic lobe area (**I**) and cortex/medullary area ratio (**L**) showed a decrease in $Smn^{2B/-}$ thymus compared to wild type thymus at P19. Scale bar represent 200 μm in A,B,G,H and 50 μm in D,E,J,K. (n = 4 for all experiments, two-tailed Student's *t* test, $P \leq 0.001$ for *** and $P \leq 0.0001$ for ****).

(DN1 - CD4^{-ve}; CD8^{-ve}, CD44$^+$, CD25^{-ve} and DN2 - CD4^{-ve}; CD8^{-ve}, CD44$^+$, CD25$^+$), gain and rearrange their T-cell antigen receptor (TCR) β before successfully pairing with pre-TCRα (DN3 - CD4^{-ve}; CD8^{-ve}, CD44^{-ve}, CD25$^+$ and DN4 - CD4^{-ve}; CD8^{-ve}, CD44^{-ve}, CD25^{-ve}) (38,40). They will then progress to CD4$^+$; CD8$^+$ cells (DP, bright - early stage, and dull - late stage) which are marked by reorganization of the α chain (38). The αβ TCR on the DP cells will be challenged for recognition to ensure that autoimmunity doesn't occur (a process known as central tolerance). T-cells that do not recognize self-antigen generally go through a mechanism known as 'neglect' while T-cells that bind strongly to self-antigen will go through negative selection (apoptosis) or anergy where they become regulatory T-cells (38,41). Therefore, only T-cells that have a receptor that have intermediate specificity to self-antigen will positively be selected (events described by co-expression of either CD5 and TCRβ or CD69 and TCRβ) and will be allowed to mature further (38). At this point, they will transiently go through CD4$^+$;CD8^{lo} stage before becoming either CD8 SP or CD4 SP mature cells and migrate to the periphery and lymphoid organs, such as the spleen (38).

Flow cytometry analysis of the P19 $Smn^{2B/-}$ thymocytes reveals major abnormalities at multiple levels of development. There was a significantly larger proportion of DN, CD4$^+$;CD8^{lo}, mature CD8 SP, and CD4 SP cells, and a diminished proportion of DP cells in $Smn^{2B/-}$ mice compared to $Smn^{2B/+}$ mice (Fig. 7A–C). This means that more cells enter the thymus and more cells go through the maturation process or that T-cells get stalled in the DN stage and mature state of development. All the population subset frequencies in the $Smn^{2B/+}$ thymus were within normal ranges for normal rodents, except for the DN population, which was slightly lower (42). Examination of the various sub-stages in the DN population showed a significant increase in the proportion of DN3 with an approximately equal decrease in the DN4 sub-population (Fig. 7D–F). The positive selection process is characterized by pre-selection (TCRβ^{lo};CD69^{-ve}), TCR engagement (TCRβ^{int};CD69$^+$), post-positive selection (TCRβ^{hi};CD69$^+$), mature positively selected SP (TCRβ^{hi};CD69^{-ve}) (38,43). Interestingly, flow cytometric analysis of the positive selection process in P19 $Smn^{2B/-}$ thymocytes identified an increase in the proportion of cells going through TCR engagement, being
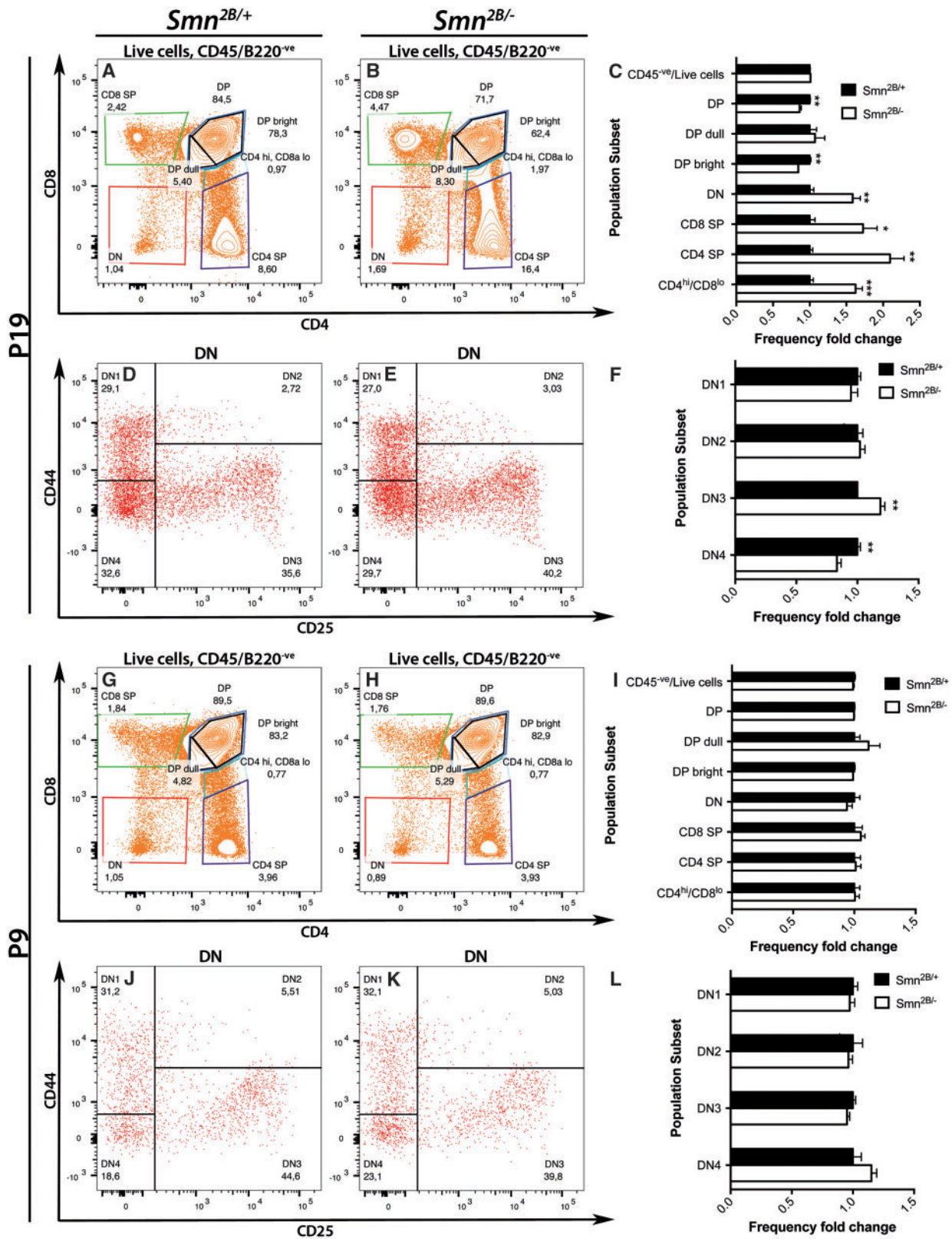
Figure 7. T-cell development is misregulated in P19 but not P9 thymus from $Smn^{2B/-}$ mice. Representative contour plots of thymocytes (gated on live cells, CD45/B220[-ve]) in various stages of development based on CD4/CD8 immunophenotyping in $Smn^{2B/+}$ and $Smn^{2B/-}$ mice at P19 (**A,B**) and P9 (**G,H**). Quantification of population frequencies presented as a fold change revealed major abnormalities at P19 (**C**) but not at P9 (**I**). Representative contour plots of DN-gated thymocytes in the various DN sub-stages based on CD44/CD25 immunophenotyping in $Smn^{2B/+}$ and $Smn^{2B/-}$ mice at P19 (**D,E**) and P9 (**J,K**). Quantification of DN sub-population frequencies presented as a fold change showed significant difference in DN3 and DN4 populations at P19 (**F**) while no change was observed at P9 (**L**). (n = 5 for P19, n = 5 and 6 for $Smn^{2B/-}$ and $Smn^{2B/+}$ respectively, two-tailed Student's *t* test, $P \leq 0.05$ for *, $P \leq 0.01$ for **, and $P \leq 0.001$ for ***).
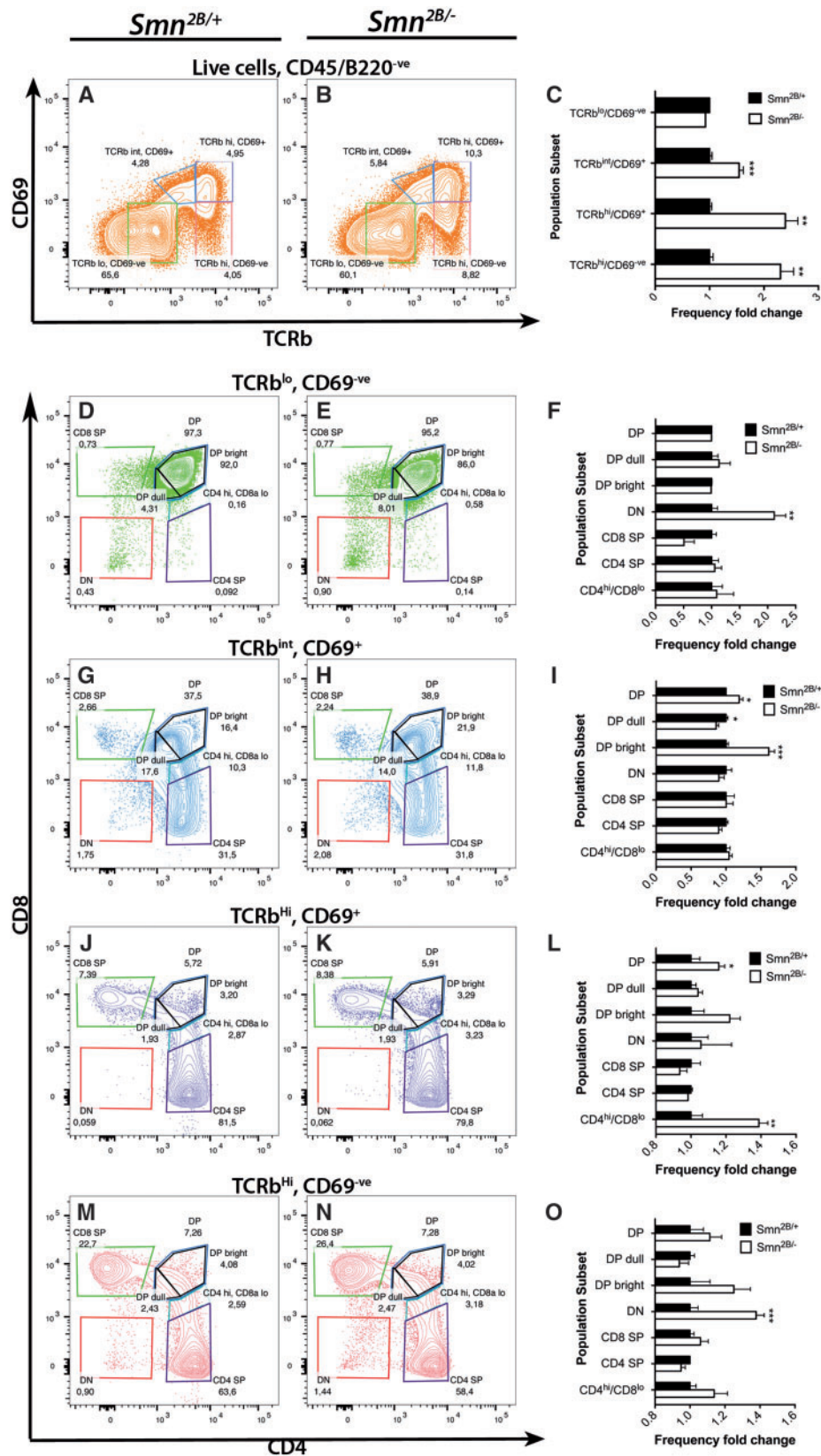
Figure 8. Precocious positive selection is present in the thymus of P19 *Smn*[2B/-] mice. Representative contour plots of thymocytes (gated on live cells, CD45/B220[-ve]) in various stages of positive selection based on CD69/TCRβ immunophenotyping in *Smn*[2B/+] and *Smn*[2B/-] mice at P19 (**A,B**). (**C**) Quantification of population frequency presented as a fold change demonstrates a significant increase in the proportion of cells going through TCR engagement (TCRβ^{int};CD69^{+}), post-positive selection (TCRβ^{hi};CD69^{+}), and mature positively selected SP (TCRβ^{hi};CD69[-ve]). Representative contour plots and quantification of sub-populations present in each positive selection stages, namely TCRβ^{lo};CD69[-ve] (D-F), TCRβ^{int};CD69^{+} (G-I), TCRβ^{hi};CD69^{+} (J-L), TCRβ^{hi};CD69[-ve] (**M-O**), by immunophenotyping cells with CD4/CD8 shows an alteration in the proportion of the sub-populations. (n = 5 for all experiments, two-tailed Student's *t* test, $P \leq 0.05$ for *, $P \leq 0.01$ for **, and $P \leq 0.001$ for ***).
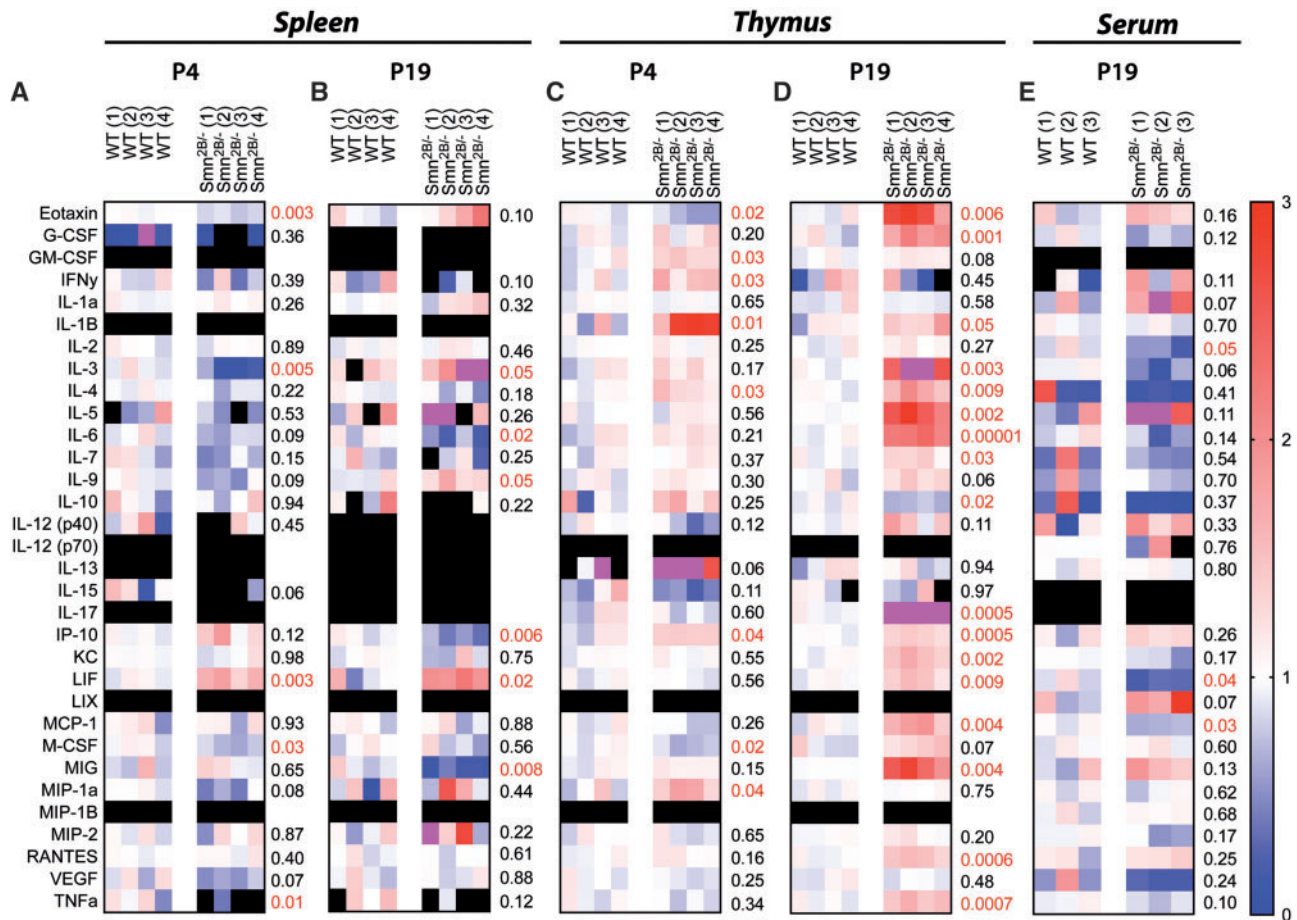
Figure 9. Cytokine profiling reveals altered protein levels in spleen and thymus from P4 and P19 *Smn*[2B/-] mice. Heat map of cytokine profiles in P4 (**A**) and P19 (**B**) *Smn*[2B/-] spleens exhibit various changes, with LIF and IL-3 being commonly misregulated at both time points. Heat map of cytokine profiles in P4 (**C**) and P19 (**D**) *Smn*[2B/-] thymus exhibit several changes, with eotaxin, IL-1B, IL-4 and IP-10 being commonly misregulated at both time points. (**E**) Heat map of cytokine profiles in serum of P19 *Smn*[2B/-] mice show down-regulation of IL-2, LIF, and MCP-1. Each box represents a fold change compared to wild type. Black boxes indicate cytokine levels too low to be sensitively recorded. Magenta boxes represent values of fold change higher than 3. The result from each individual sample is shown in the columns. (n = 4 for each experiment other than serum where n = 3, two-tailed Student's *t* test, the *P* values are indicated next to the heat maps).

positively selected and being more mature (Fig. 8A–C). The analysis of sub-populations of cells going through these events was mostly unremarkable, except for an increase in the proportion of DN cells appearing as mature TCRβ^{hi};CD69[-ve] cells (Fig. 8D–O). Alternately, analysis of positive selection through CD5 and TCRβ surface marker expression yielded similar results (Supplementary Material, Fig. S7). These results point towards a precocious positive cell selection, potentially to increase mature naïve T-cell production.

We next examined whether these changes occurred at an earlier time point. Surprisingly, flow cytometry analysis of P9 *Smn*[2B/-] thymocytes revealed no significant abnormalities in the proportion of sub-populations compared to *Smn*[2B/+] thymocytes (Fig. 7G–L). Similarly, very few changes were observed in the positive selection process analysed by TCRβ with either CD69 or CD5 (Supplementary Materials, Figs S8 and S9) Therefore, it appears that the changes in the thymocyte cell populations in P19 *Smn*[2B/-] mice are either independent to the spleen defects or a consequence in response to abnormalities in the periphery such as in the spleen. We attempted to perform a similar flow cytometry analysis to characterize immune sub-populations in spleens from P19 and P9 *Smn*[2B/-] mice but were unsuccessful in retrieving enough cells due to their small size.

Cytokine profiles are altered in lymphoid organs of SMA model mice

To better understand the functional impairments and/or the aetiology of the defects observed in the lymphoid organs, a thorough cytokine screen in the thymus and spleen at P4 and P19, and in the serum at P19 was performed (Fig. 9). It is important to note that naïve cytokine levels are often very low, if even measurable. To our surprise, many changes were readily detected in every organ and time point analysed. The greatest changes were observed in P19 thymus from *Smn*[2B/-] mice, with almost a global increase of many of the cytokines screened (Fig. 9D). Interestingly, a very similar heat map profile was apparent in P4 thymus (Fig. 9C). Given the reduction in spleen size, we expected an inflammatory profile, indicative of cell death. However, none of the inflammatory cytokines (such as IL-1β, IL-6, and TNF-α) were significantly changed in both P4 and P19 *Smn*[2B/-] spleens (Fig. 9A and B). On the other hand, the thymus of P19 *Smn*[2B/-] mice showed significant induction of many inflammatory cytokines such as IL-1β, IL-6 and TNF-α (Fig. 9D). We also noticed that some cytokines appeared misregulated in more than one organ. Notably, eotaxin, IL-3, IL-6, IP-10, LIF, MIG were misregulated in spleen and thymus (Fig. 9A–D). Similar analysis of *Smn*[2B/-] P19 lymph nodes revealed that LIF levels

were significantly changed (Supplementary Material, Fig. S10A). Changes in IL-2, M-CSF, VEGF, and TNF-α were also present (Supplementary Material, Fig. S10A). We also investigated the cytokine profile of spinal cord tissue (Supplementary Material, Fig. S10B). Once again, eotaxin and IP-10 expression was altered (Supplementary Material, Fig. S10B). A trend towards an inflammatory profile was present with a mild increase in IL-1β, MIP1α and TNF-α, however many did not reach significance (Supplementary Material, Fig. S10B).

The spleen and thymus of P5 $Smn^{-/-}$;SMN2 mice were also subjected to cytokine profiling (Supplementary Material, Fig. S10C and D). Strikingly, eotaxin, IP-10 and MIG were misregulated in P5 $Smn^{-/-}$;SMN2 spleens while IP-10, LIF, and MIG were significantly changed in the thymus (Supplementary Material, Fig. S10C and D). These changes, however, were not always in the same direction, once again highlighting the molecular complexities between different severities of disease. The P5 $Smn^{-/-}$;SMN2 thymus and spleen also display common cytokine changes not displayed in the $Smn^{2B/-}$ model mice. More particularly, VEGF was increased compared to wild type in both spleen and thymus while IL-9 showed changes in the opposite direction (Supplementary Material, Fig. S10). Altogether, the extent of changes observed highlight the intense pathology in the lymphoid organs and the potential consequence it may have in overall immune function.

SMN expression in lymphoid organs

Smn expression in the lymphoid tissues of wild type mice was compared to other commonly affected tissues in SMA such as skeletal muscle and spinal cord. When compared to skeletal muscle, both thymus and spleen had strikingly higher Smn protein levels at P19 (Fig. 10A and B). Interestingly, Smn protein levels in the lymphoid tissues were even higher than in the spinal cord (Fig. 10A and B). It is recognized that *Smn* levels are generally high embryonically and decrease gradually after birth in most tissues studied (44). Smn protein levels in wild type spleens were fairly similar from P0 to P14 with an increase P14 to P19 (Fig. 10C). Moreover, Smn levels closely followed the expression pattern of CD3 and CD19, which are T-cell and B-cell markers respectively. In the thymus, Smn protein levels were sustained from P0 to P19 (Fig. 10D). As expected, we observed significantly reduced levels of Smn protein in both $Smn^{2B/-}$ spleen and thymus in comparison to wild type (Fig. 10E).

Genetic introduction of one copy of SMN2 rescues lymphoid organ defects in Smn$^{2B/-}$ mice

To determine whether lymphoid organ defects were directly caused by low levels of Smn protein, we crossed the $Smn^{2B/2B}$ mouse to a $Smn^{+/-}$;SMN2$^{+/+}$ mouse. The progeny from this cross would contain $Smn^{2B/-}$;SMN2 mice, allowing for a slight increase in SMN protein from the newly introduced human *SMN2* transgene. Surprisingly, we observed a complete rescue in the size of the spleen and the thymus on gross morphology assessment at P19 (Fig. 11A,D,G). In addition, the structure of the spleen was comparable to wild type mice on histology at this age, with multiple white pulp areas readily evident (Fig. 11B and C). H&E analysis of the thymus similarly showed no differences in the rescued mice when compared to wild type (Fig. 11E and F). Western blot analysis showed a modest increase in Smn protein levels in $Smn^{2B/-}$;SMN2 mice compared to $Smn^{2B/-}$ mice (Fig. 11H).

Discussion

The immune system has not been extensively studied in SMA, but defects in such cells could lead to immune deficiencies or enhance neuroinflammation. In fact, altered immune function in SMA patients could exacerbate disease progression and result in increased hospitalization rate, longer hospital stay, increased morbidity and mortality. However, given the compromised health status and the multiple interventions that SMA patients go through, it is likely that immune involvement, if present, has been historically considered part of the secondary effects and not attributed to disease pathogenesis per se. Here, we report smaller lymphoid organs in two mouse models of SMA. Tissue architectural abnormalities were observed in the thymus of both symptomatic $Smn^{2B/-}$ and $Smn^{-/-}$;SMN2 mice and in the spleen in $Smn^{2B/-}$ mice. Importantly, we also report aberrations in T-cell development in P19 stage $Smn^{2B/-}$ mice, and cytokine level alterations in multiple contexts in both $Smn^{2B/-}$ and $Smn^{-/-}$;SMN2 mice, which could have important functional consequences.

Neuroinflammation is a well-established contributor in neurodegenerative disorders (45). Peripheral immune alterations have surfaced in the amyotrophic lateral sclerosis (ALS) field. Interestingly, G93A SOD1 ALS mouse models showed reduced spleen size, architectural defects, and increase cell death of the splenic T-cells and B-cells (46). Moreover, healthy immune cell transplantation lead to better motor performance and survival (46). A new potential model for ALS, the C9orf72 knockout mouse, presented with splenomegaly and enlarged lymph nodes, marked by malfunctioning macrophages and microglia as early pathologic features (47). Subsequently, neuroinflammation appeared with age and molecularly resemble, at the transcriptome level, that of C9-ALS human patients (47). Interestingly, T-cells appear to be an important player in the neuroprotection conferred by glial cells in ALS (48,49). It is possible that the pre-symptomatic defects we observed in the spleen are caused by immune cell-autonomous defects. Thus, dysfunctional T-cells and potentially other cell types may limit the full neuroprotective potential of the glial system in the context of SMA. In a similar manner, the spleen size observed is likely to evoke an immune cell redistribution to the circulating system, which may have peripheral consequences.

Even though the thymus was relatively spared as evidenced from the morphological assessment, its architecture was abnormal in both mouse models of SMA, albeit to different degrees of severity. Interestingly, the thymus had the highest Smn protein expression compared to spleen, spinal cord and skeletal muscle, and this expression was relatively sustained over time. Moreover, the thymus from $Smn^{2B/-}$ mice showed severe corticomedullary thinning in comparison to those from the $Smn^{-/-}$;SMN2 mice. Interestingly, an increased proportion of apoptotic bodies and tingible body macrophages were also present in both mouse models of SMA, suggestive of active apoptotic or necrotic processes (39). This appears to be in accordance with a previous report showing increased cell death in $Smn^{-/-}$;SMN2 thymocytes (34). In addition, we found the increased proportion of mature SP thymocytes (residents of the medulla) and decreased the proportion of DP thymocytes (residents of the cortex) on flow cytometry analysis, which nicely fits with the cortico-medullary thinning. Studies have shown that administration of glucocorticoids leads to similar changes in population proportions (50,51). Additionally, increased glucocorticoid levels could also be responsible for the increase in apoptotic bodies we observed in the cortex, more specifically in
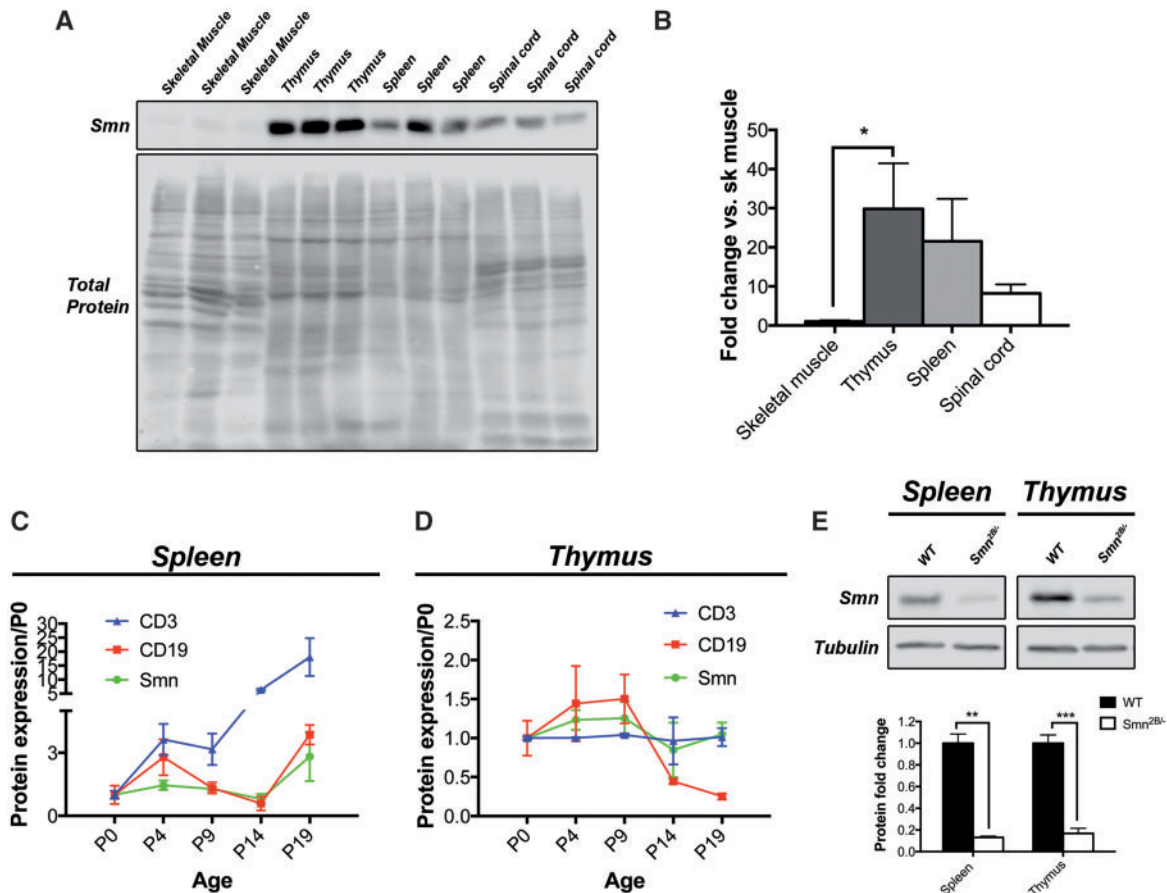
Figure 10. High levels of Smn protein in lymphoid organs during postnatal development. (**A**) Western blot analysis of Smn in different tissues of P19 wild type mice. The membrane stained for total protein is shown in the panel below. (**B**) Quantification of the western blot highlights the relative high Smn protein expression in the thymus and in the spleen compared to skeletal muscle and spinal cord. (**C**) Quantification of western blot analysis of the temporal protein expression profile of CD3, CD19 and Smn in spleen from wild type mice shows a relatively sustained Smn expression that is similar to CD3 and CD19. (**D**) Quantification of western blot analysis of the temporal protein expression profile of CD3, CD19 and Smn in thymus from wild type mice shows sustained expression for all three proteins. (**E**) Smn levels in the $Smn^{2B/-}$ spleen and thymus were reduced as expected. (n = 3 in A and B, n = 2 for each time point in C and D, and n = 4 for E. One-way ANOVA with bonferroni post-test for B and two-tailed Student's *t* test for E, $P \leq 0.05$ for *, $P \leq 0.01$ for **, and $P \leq 0.001$ for ***).

the DP population (39,52). In addition to changes in population proportions, a higher proportion of $Smn^{2B/-}$ thymocytes were precociously going through the positive selection process. It is possible that this is in response to a loss of peripheral T-cell homeostasis. T-cells could be going through precocious apoptosis in secondary lymphoid organs. Related to this, we have observed hyperchromaticity in P19 $Smn^{2B/-}$ spleens, which is generally a sign of apoptotic processes.

The triggering event that causes the spleen to become small and display an abnormal architecture remains to be determined. We hypothesized that the T-cells may be stalled in the thymus, consequently not migrating to the spleen. Our analysis of thymic histological changes and T-cell development revealed that these changes occur later (P19) than any defects in the spleen (P4). Autonomic dysfunction has been reported in SMA (17–20,53–55). Importantly, spleen and thymus architecture may also be dependent on neuronal signals (56,57). Autonomic dysfunction or denervation could be a potential cause for abnormal compartmentalization within the spleen in SMA. Chemokines have also been shown to be important for recent emigrant thymocytes to travel to secondary lymphoid organs (a process known as homing) (32,58). For example, manipulating lymphotoxin α/β, CCL19 and CCL21 or their receptors lead to splenic

architectural disruption (59–65). Altogether, examining the interaction between the primary and secondary lymphoid organs by studying the immune system as a whole will be crucial to understanding and correctly interpreting the abnormalities observed.

The architecture of the spleen is complex and highly organized to ensure efficiency of its multiple functions. The spleen can exert both innate and adaptive immune response in the presence of an unknown pathogen, especially if present in the blood (32). This is facilitated by the fact that most of the blood travels in the marginal zone, where different populations of macrophages, dendritic cells and B-cells reside (32). These macrophages are particularly important in the clearance of pathogens like *Mycobacterium tuberculosis*, *Streptococcus pneumoniae*, *Escherichia coli*, *Staphylococcus aureus*, and *Neisseria meningitidis* through the innate arm of the immune system (32,66–69). On the other hand, the marginal zone B-cells can readily become antibody-producing cells if they come across a foreign antigen and migrate in the red pulp for fast antibody delivery into the bloodstream (32). They can also become antigen presenting cells (APCs) and migrate to the white pulp where they activate a T-cell dependent response as part of the adaptive immune system (32). A disruption of the splenic architecture as observed in the
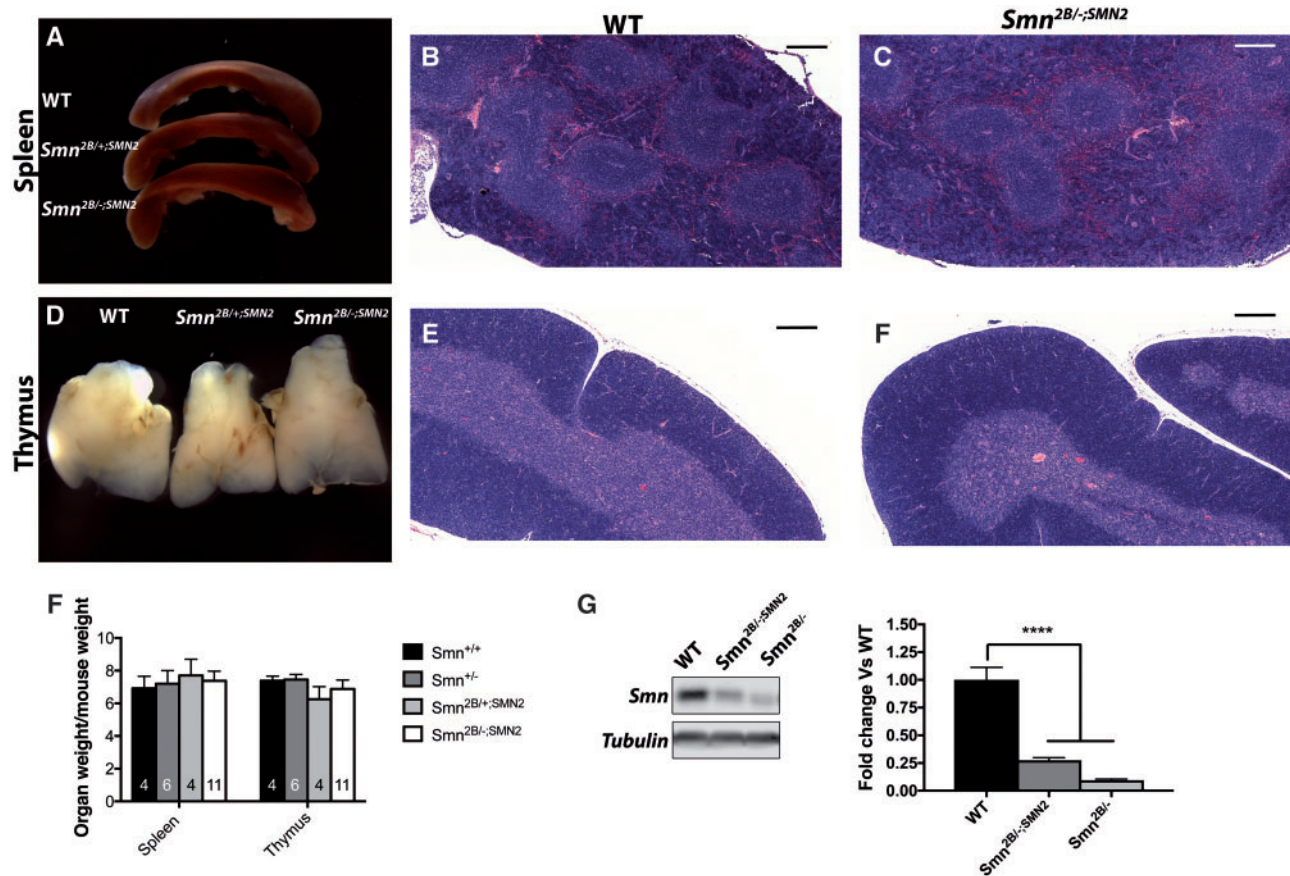
Figure 11. Genetic introduction of the human *SMN2* transgene in the *Smn*[2B/-] mice rescues the lymphoid organ defects. Gross morphology of the spleen and the thymus are rescued in the *Smn*[2B/-];*SMN2* mice at P19 (**A,D,G**). H&E staining of the *Smn*[2B/-];*SMN2* spleen shows structural integrity with the presence of white pulp comparable to wild type (**B,C**). H&E staining of the *Smn*[2B/-];*SMN2* thymus shows rescue of the cortex thinning (**E,F**). Smn protein levels in the spinal cord of the *Smn*[2B/-];*SMN2* mouse is modestly increased relative to *Smn*[2B/-] , but still lower than wild type (**H**). (The n value for A,D,G are as written in the graph bars of G, $n = 3$ in B,C,E,F, and $n = 4$ for H, one-way ANOVA with bonferroni post-test for F,G, $P \leq 0.0001$ for ****).

Smn[2B/-] mice is likely to impair some, if not many, of the processes described above. The loss of proper white pulp formation could have several possible consequences. For example, it is unknown whether the marginal zone is still present around the 'absent' white pulp. Interestingly, we noticed that the residents of this zone, namely the B-cells and macrophages, showed diffuse localization throughout the spleen. The T-cells were also found diffusely distributed across the whole spleen. The red pulp, an area where T-cells are generally not found, could be absent. The red pulp is responsible for clearance of old erythrocytes and for iron homeostasis (32). This could lead to haematological abnormalities. Future research is needed to better understand the defective architecture of the spleen and the specific functional impairments of *Smn*[2B/-] mice by the characterization of the different populations of macrophages, dendritic cells, T-cells and B-cells.

The accumulation of smooth muscle cells in the P19 *Smn*[2B/-] spleens is rather intriguing. Smooth muscle cells are normally found around arteries and within organs. It is possible that abnormal blood vessel morphogenesis leads to less extensive artery and capillary network, and consequently results in a higher probability of splenic infarct in the *Smn*[2B/-] mice. It is now evident that distal necrosis is a prominent feature of mouse models of SMA, especially when therapeutics allow for lifespan extension (8,70–72). Some SMA patients also display similar

features (54,55). Moreover, blood vessel abnormalities have been shown in skeletal muscles, hearts and the spinal cord (20,73,74). Since the spleen is engorged with red blood cells, it is possible that a lower perfusion efficiency could explain the decreased spleen size, architectural abnormalities and the trend of higher incidence of splenic infarct.

The cytokine profiling revealed global immune dysregulation, which could have severe functional consequences. Surprisingly, despite the phenotype observed, the spleen of the *Smn*[2B/-] model mice did not show a very strong inflammatory profile as assessed by expression of inflammatory cytokines such as IL-1β, IL-6, and TNF-α (75). In marked contrast, the thymus showed marked inflammatory cytokine expression and a decrease in the anti-inflammatory cytokine IL-10. Interestingly, some of these changes were present in *Smn*[2B/-] P4 thymus. LIF, a cytokine in the IL-6 family, which is considered an inflammatory cytokine (75), is misregulated in multiple organs and time points. Even though very few histological changes were observed in the P5 *Smn*[−1−];*SMN2* spleen, changes in G-CSF, GM-CSF seem to point towards increased hematopoiesis. This clear disruption in cytokine homeostasis accentuates the potential role of immune dysfunction in SMA pathogenesis. Altogether, we presented an array of abnormalities in various lymphoid organs in mouse models of SMA. Whether these alterations directly increase neuroinflammation or result in immune

deficiencies, remains to be determined. Future research will focus on narrowing potential aetiologies of such defects and investigating functional impairments of defective lymphoid organs in the SMA context.

Materials and Methods

Mouse models

The $Smn^{-/-}$;SMN2 (Jackson Laboratory) and $Smn^{2B/-}$ (C57BL/6J background) (36) mouse lines were housed at the University of Ottawa Animal Facility and cared for according to the Canadian Council on Animal Care. $Smn^{+/-}$ mice (C57BL/6J) were crossed to $Smn^{2B/2B}$ mice (C57BL/6J) to obtain $Smn^{2B/+}$ and $Smn^{2B/-}$ animals. Similarly, $Smn^{+/-}$;SMN2$^{+/+}$ (FVB) mice were crossed to $Smn^{2B/2B}$ (FVB) mice to obtain $Smn^{2B/+}$;SMN2 and $Smn^{2B/-}$;SMN2 (FVB) animals (36). C57BL/6J and FVB wild type mice were bred separately. Spleen and thymus were harvested from pre-symptomatic (P0 and P2) and symptomatic (P5) $Smn^{-/-}$;SMN2 mice. Tissues were collected at P0, P4 and P9 pre-symptomatic mice and from P14 and P19 symptomatic $Smn^{2B/-}$ and $Smn^{2B/-}$;SMN2 mice.

Gross morphology

A 0.75X picture of the spleens and tibia were taken with a Leica M80 dissection microscope mounted with a camera (Leica IC80 HD). The lengths of the spleen were measured using ImageJ. The mouse measurements for normalization were done prior to dissection using a ruler for the length of the mouse and a scale for its weight. Tissues were then fixed in 10% formalin for 24-48 h and transferred to 70% ethanol for long-term storage.

Tissue processing and H&E staining

Spleens, thymus and lymph nodes were fixed in formalin (1:10 dilution buffered, from Protocol, cat #245-684) for 24-48 h at 4°C and then transferred in 70% ethanol at 4°C until processing. All samples were processed at the University of Ottawa (Department of Pathology and Laboratory Medicine) and embedded in wax using a LOGOS microwave hybrid tissue processor. Paraffin block tissues were cut with a microtome at 3-4 μm of thickness and stained for H&E using a Leica autostainer XL Leica CV5030. Stained H&E samples were scanned with a MIRAX MIDI digital slide scanner (Zeiss). Images were acquired using 3DHISTECH Panoramic Viewer 1.15.4 at different magnifications. Quantification of the thymus area and the corticomedullary area ratio was performed by assessing area of 3 serially cut sections (slide 5, 10 and 15 or 17) using ImageJ. One or both lobes per slide were quantified depending whether both lobes were present on the slide.

Immunohistochemical staining

Tissues were processed, embedded and sectioned as described above. Slides were deparaffinized in 3 changes of xylene substitute HEMO-DE (Electron Microscopy Science, 23412-01) (or toluene) for 5 min each followed by 2 changes into a 50/50 mixture of absolute ethanol and HEMO-DE (or toluene) for 5 min each. Slides were gradually rehydrated in 100%-95%-70%-50%-0% ethanol. A heat-induced antigen retrieval step was performed when needed using Tris/EDTA buffer (10 mM Tris, 1 mM EDTA, 0.05% Tween 20, pH 9.0) or sodium citrate pH 6.0. Sections were permeabilized with 0.1% Triton-X (Sigma) and then blocked for

1 h in 5-10% goat serum in PBS for 1 h. M.O.M kit (Vector, BMK-2202) was used as per the manufacturer's protocol to optimize staining condition of primary mouse antibodies on mouse primary tissue. Slides were incubated with primary antibodies for 90 min at room temperature at the following concentrations: CD3 (DAKO #2018-11 - 1:100), CD19 (Abcam, ab197895 or ab31947 - 1:100) and F4/80 (eBioscience ref 14-4801 - 81–1:100 or Abcam, ab6640 - 1:100) and cleaved caspase 3 (Cell signalling, 9664L - 1:300). For TUNEL (Roche, 11684795910) staining, manufacturer's instructions were followed. Sections were washed and then incubated with secondary antibodies (Alexa Fluor-488, Alexa Fluor-555 or Alexa Fluor-647 from Invitrogen - 1:500) for 1 h at room temperature. Sections counterstained with 33-diamino-benzidine (DAPI, Molecular Probes, D1306). Slides were mounted with fluorescent mounting medium (DAKO mounting media). Pictures were acquired using microscope Zeiss Axio Imager M1 mounted with a camera.

Immunoblotting

The total protein lysate was collected by homogenization of flash frozen spleen, thymus, lymph nodes, skeletal muscle, or spinal cord in RIPA lysis buffer (Cell Signalling). Protein concentrations were determined using the Bradford assay (Bio-Rad). Protein extracts were subjected to sodium dodecyl sulphate polyacrylamide gel electrophoresis and examined by immuno-blot, as previously described (76) with modified blocking conditions where Odyssey blocking buffer (Li-Cor 927-40000) replaced 5% milk. Revert Total protein stain (Li-Cor 926-11010) was used as per the manufacturer's protocol. Primary antibodies used were as follows: Anti-Smn (BD Transduction, 610647 - 1:2000), CD3 (DAKO #2018-11 - 1:1000), CD19 (Abcam, ab197895 - 1:1000) and alpha-tubulin (Abcam, ab4074 – 1:1000). Secondary antibodies used were IRDye 680 or 800 (Li-Cor - 1:10000 to 1:20000). Signals were detected with Odyssey CLx (Li-Cor). The results were normalized to total protein or tubulin.

RNA isolation and reverse transcription-quantitative polymerase chain reaction (RT-QPCR)

Total RNA was extracted from mouse models of SMA and wild type controls using RNeasy kit (Qiagen) according to the manufacturer's protocol. RNA concentrations were determined using a Nanophotometer spectrophotometer (MBI Lab Equipment). RNA was reversed transcribed using the quantitect reverse-transcription kit (Qiagen) according to the manufacturer's protocol. QPCR was performed in triplicate. A complete list of primers are available in the Supplementary Material (Supplementary Material, Table S1). A standard curve was performed for each primer set to ensure their efficiency. Each QPCR reaction contained equal amount of cDNA, Ssofast Evagreen Supermix (Biorad), RNase/DNase-free water and appropriate primers (100–200 nM) in a final volume of 25 μl. Two negative controls were included in every QPCR plate and consisted of water in lieu of cDNA. QPCR results were analysed using Biorad CFX manager 3.1. Results were normalized to two or three internal controls that were determined to have stable expression according to their M-value (below 0.5) and their coefficient variance (below 0.25). The internal controls for each experiment are as follows: P2 thymus (Cyclophilin A and PBGD), P5 thymus (PBGD and SDHA), P4 thymus (PolJ, Hprt1, PBGD), and P19 thymus (Ubiquitin C and Ywhaz).

Cell extraction and flow cytometry

Thymus were dissected from mice and put directly in R10 (89.4% 1X RPMI media 1640 (Gibco, 11875-168), 10% fetal bovine serum (Life Science Seradigm, 97068-085), 0.5% gentamycin (Gibco, 15710-072), 0.1% 2-mercaptoethanol (Gibco, 21985-023)) until further processing. Once all samples were collected, tissues were squashed between two frosted slides to obtain a single cell suspension. The single cell suspension was then passed through a 100 μm and a 70 μm strainer to ensure the remaining tissue aggregates were left behind and spun at 500 g for 5 min. The cells were further resuspended in 1X BD Pharm Lyse (BD Biosciences, 555899) for 5 min and then washed twice with PBS. Cells were counted and an equal number of cells was placed in each tube for flow cytometry analysis. Samples were first stained with fixable viability stain 510 (BD Biosciences, 564406) according to the manufacturer's protocol. Cells were resuspended in staining buffer (1% bovine serum albumin) and incubated with FcBlock (BD Pharmingen, 553142) for 10 min at 4°C. The following antibodies (BD Biosciences) CD69 (740664 - 1:400), CD44 (563058 - 1:400), CD5 (562739 - 1:100), CD45/B220 (561101 - 1:100), CD4 (561835 - 1:400), TCRβ (560729 - 1:400), CD25 (562695 - 1:400), and CD8a (561095 - 1:100) were added to the suspension and incubated for 30 min in the dark at 4°C. The samples were then washed with staining buffer. Cells were resuspended in 1:1 staining buffer and IC fixation buffer (eBioscience, 00-8222-49). Samples were acquired by the flow cytometry core (BD LSR Fortessa flow cytometer) of the University of Ottawa within 2 days of being stained. Single stain controls were performed with OneComp ebeads (eBioscience, 01-1111-42) as per the manufacturer's protocol and were then used to set the flow cytometer parameter. Fluorescence-minus-one were also performed in parallel and acquired in similar fashion as the samples to ensure correct identification of populations. P19 thymus acquisition was stopped once 10,000 events were acquired in the DN gate while P9 thymus acquisition was stopped once 3,000 events were acquired in the DN gate to ensure enough events for proper quantification.

Cytokine profiling

Mouse blood was obtained by cardiac puncture from wild type and $Smn^{2B/-}$ mice at P19. Blood was left at room temperature for 1-2 hours before centrifugation at 10,000 g for 10 min at 4°C to obtain serum (as per Eve Technologies' instructions). Serum was diluted in a 1:1 ratio with PBS for analysis. Spleens, thymus, and lymph nodes were collected and protein was extracted as described above. All protein lysates were diluted at a concentration of 1 μg/μL in a total of 80 μL for duplicate analysis. Serum and protein lysates were shipped to Eve Technologies for cytokine profiling. We quantified 32 cytokine/chemokine/growth factor biomarkers simultaneously by using a Discovery Assay® called the Mouse Cytokine Array/Chemokine Array 32-Plex (Eve Technologies Corp, Calgary, AB, Canada). The multiplex assay was performed by using the Bio-Plex TM 200 system (Bio-Rad Laboratories, Inc., Hercules, CA, USA), and a Milliplex Mouse Cytokine/Chemokine kit (Millipore, St. Charles, MO, USA) according to their protocol. The 32-plex consisted of eotaxin, G-CSF, GM-CSF, IFNγ, IL-1α, IL-1β, IL-2, IL-3, IL-4, IL-5, IL-6, IL-7, IL-9, IL-10, IL-12 (p40), IL-12 (p70), IL-13, IL-15, IL-17, IP-10, KC, LIF, LIX, MCP-1, M-CSF, MIG, MIP-1α, MIP-1β, MIP-2, RANTES, TNFα, and VEGF. The assay sensitivities of these markers range from 0.1-33.3 pg/mL. Individual analyte values and other assay details are available on Eve Technologies' website or in the Milliplex

protocol. Analytes that were undetectable were defined as 0 pg/mL and labelled as a black box. Extrapolated results were included in the analysis. When analytes were undetectable in all or most animals from both control and SMA mice, analysis were not performed and also represented as a black box in the heat maps (Fig. 9 and Supplementary Material, Fig. S10).

Statistics

Data are presented as the mean ± standard error of the mean. A two-tailed Student's *t* test was performed using Microsoft Excel or Graphpad Prism 7 to compare the means of data when only two groups were compared (i.e. wild type vs. $Smn^{2B/-}$). Splenic infarct relative risk was assessed by a Fischer's exact test and confidence interval calculated by Koopman asymptotic score. One-way ANOVA analysis was used to distinguish differences between more than two groups when multiple comparisons were necessary (i.e. wild type vs. $Smn^{2B/+}$ vs. $Smn^{2B/-}$). The post-test used for the ANOVA was Bonferroni. Significance was set at $P \leq 0.05$ for *, $P \leq 0.01$ for **, $P \leq 0.001$ for *** and $P \leq 0.0001$ for ****.

Study approval

This study was approved by the Animal Care and Veterinary Services (ACVS) of the University of Ottawa as specified by protocol #OHRI-1927 and #OHRI-1948.

Supplementary Material

Supplementary Material is available at *HMG* online.

References

1. Lefebvre, S., Bürglen, L., Reboullet, S., Clermont, O., Burlet, P., Viollet, L., Benichou, B., Cruaud, C., Millasseau, P. and Zeviani, M. (1995) Identification and characterization of a spinal muscular atrophy-determining gene. *Cell*, **80**, 155–165.
2. Liu, Q., Fischer, U., Wang, F. and Dreyfuss, G. (1997) The spinal muscular atrophy disease gene product, SMN, and its associated protein SIP1 are in a complex with spliceosomal snRNP proteins. *Cell*, **90**, 1013–1021.

3. Pellizzoni, L., Kataoka, N., Charroux, B. and Dreyfuss, G. (1998) A novel function for SMN, the spinal muscular atrophy disease gene product, in pre-mRNA splicing. *Cell*, **95**, 615–624.

4. Boyer, J.G., Bowerman, M. and Kothary, R. (2010) The many faces of SMN: deciphering the function critical to spinal muscular atrophy pathogenesis. *Future Neurol.*, **5**, 873–890.

5. Hamilton, G. and Gillingwater, T.H. (2013) Spinal muscular atrophy: going beyond the motor neuron. *Trends Mol. Med.*, **19**, 40–50.

6. Shababi, M., Lorson, C.L. and Rudnik-Schöneborn, S.S. (2014) Spinal muscular atrophy: a motor neuron disorder or a multi-organ disease?. *J. Anat.*, **224**, 15–28.

7. Hua, Y., Sahashi, K., Rigo, F., Hung, G., Horev, G., Bennett, C.F. and Krainer, A.R. (2011) Peripheral SMN restoration is essential for long-term rescue of a severe spinal muscular atrophy mouse model. *Nature*, **478**, 123–126.

8. Hua, Y., Liu, Y.H., Sahashi, K., Rigo, F., Bennett, C.F. and Krainer, A.R. (2015) Motor neuron cell-nonautonomous rescue of spinal muscular atrophy phenotypes in mild and severe transgenic mouse models. *Genes Dev.*, **29**, 288–297.

9. McGivern, J.V., Patitucci, T.N., Nord, J.A., Barabas, M.E.A.E., Stucky, C.L. and Ebert, A.D. (2013) Spinal muscular atrophy astrocytes exhibit abnormal calcium regulation and reduced growth factor production. *Glia*, **61**, 1418–1428.

10. Rindt, H., Feng, Z., Mazzasette, C., Glascock, J.J., Valdivia, D., Pyles, N., Crawford, T.O., Swoboda, K.J., Patitucci, T.N., Ebert, A.D., *et al.* (2015) Astrocytes influence the severity of spinal muscular atrophy. *Hum. Mol. Genet.*, **24**, 4094–4102.

11. Shafey, D., Côté, P.D. and Kothary, R. (2005) Hypomorphic Smn knockdown C2C12 myoblasts reveal intrinsic defects in myoblast fusion and myotube morphology. *Exp. Cell Res.*, **311**, 49–61.

12. Hayhurst, M., Wagner, A.K., Cerletti, M., Wagers, A.J. and Rubin, L.L. (2012) A cell-autonomous defect in skeletal muscle satellite cells expressing low levels of survival of motor neuron protein. *Dev. Biol.*, **368**, 323–334.

13. Boyer, J.G., Deguise, M.O.O., Murray, L.M., Yazdani, A., De Repentigny, Y., Boudreau-Larivière, C. and Kothary, R. (2014) Myogenic program dysregulation is contributory to disease pathogenesis in spinal muscular atrophy. *Hum. Mol. Genet.*, **23**, 4249–4259.

14. Boyer, J.G., Murray, L.M., Scott, K., De Repentigny, Y., Renaud, J.M.M. and Kothary, R. (2013) Early onset muscle weakness and disruption of muscle proteins in mouse models of spinal muscular atrophy. *Skeletal Muscle*, **3**, 24.

15. Deguise, M.O.O., Boyer, J.G., McFall, E.R., Yazdani, A., De Repentigny, Y. and Kothary, R. (2016) Differential induction of muscle atrophy pathways in two mouse models of spinal muscular atrophy. *Sci. Rep.*, **6**, 28846.

16. Bricceno, K.V., Martinez, T., Leikina, E., Duguez, S., Partridge, T.A., Chernomordik, L.V., Fischbeck, K.H., Sumner, C.J. and Burnett, B.G. (2014) Survival motor neuron protein deficiency impairs myotube formation by altering myogenic gene expression and focal adhesion dynamics. *Hum. Mol. Genet.*, **23**, 4745–4757.

17. Heier, C.R., Satta, R., Lutz, C. and DiDonato, C.J. (2010) Arrhythmia and cardiac defects are a feature of spinal muscular atrophy model mice. *Hum. Mol. Genet.*, **19**, 3906–3918.

18. Bevan, A.K., Hutchinson, K.R., Foust, K.D., Braun, L., McGovern, V.L., Schmelzer, L., Ward, J.G., Petruska, J.C., Lucchesi, P.A., Burghes, A.H., *et al.* (2010) Early heart failure in the SMNDelta7 model of spinal muscular atrophy and

19. correction by postnatal scAAV9-SMN delivery. *Hum. Mol. Genet.*, **19**, 3895–3905.

19. Shababi, M., Habibi, J., Ma, L., Glascock, J.J., Sowers, J.R. and Lorson, C.L. (2012) Partial restoration of cardio-vascular defects in a rescued severe model of spinal muscular atrophy. *J. Mol. Cell. Cardiol.*, **52**, 1074–1082.

20. Shababi, M., Habibi, J., Yang, H.T., Vale, S.M., Sewell, W.A. and Lorson, C.L. (2010) Cardiac defects contribute to the pathology of spinal muscular atrophy models. *Hum. Mol. Genet.*, **19**, 4059–4071.

21. Bowerman, M., Michalski, J.P.P., Beauvais, A., Murray, L.M., DeRepentigny, Y. and Kothary, R. (2014) Defects in pancreatic development and glucose metabolism in SMN-depleted mice independent of canonical spinal muscular atrophy neuromuscular pathology. *Hum. Mol. Genet.*, **23**, 3432–3444.

22. Bowerman, M., Swoboda, K.J., Michalski, J.P.P., Wang, G.S.S., Reeks, C., Beauvais, A., Murphy, K., Woulfe, J., Screaton, R.A., Scott, F.W., *et al.* (2012) Glucose metabolism and pancreatic defects in spinal muscular atrophy. *Ann. Neurol.*, **72**, 256–268.

23. Wang, C.H., Finkel, R.S., Bertini, E.S. and Schroth, M. (2007) Consensus statement for standard of care in spinal muscular atrophy. *J. Child Neurol.*, **22**, 1027–1049.

24. Gombash, S.E., Cowley, C.J., Fitzgerald, J.A., Iyer, C.C., Fried, D., McGovern, V.L., Williams, K.C., Burghes, A.H., Christofi, F.L., Gulbransen, B.D., *et al.* (2015) SMN deficiency disrupts gastrointestinal and enteric nervous system function in mice. *Hum. Mol. Genet.*, **24**, 3847–3860.

25. Sintusek, P., Catapano, F., Angkathunkayul, N., Marrosu, E., Parson, S.H., Morgan, J.E., Muntoni, F. and Zhou, H. (2016) Histopathological Defects in Intestine in Severe Spinal Muscular Atrophy Mice Are Improved by Systemic Antisense Oligonucleotide Treatment. *PloS One*, **11**,

26. Bürglen, L., Spiegel, R., Ignatius, J., Cobben, J.M., Landrieu, P., Lefebvre, S., Munnich, A. and Melki, J. (1995) SMN gene deletion in variant of infantile spinal muscular atrophy. *The Lancet*, **346**,

27. Menke, L.A., Poll-The, B.T. and Clur, S.A. (2008) Congenital heart defects in spinal muscular atrophy type I: a clinical report of two siblings and a review of the literature. *Am. J. Med. Genet. A*, **146A**, 740–744.

28. Tein, I., Sloane, A.E., Donner, E.J., Lehotay, D.C., Millington, D.S. and Kelley, R.I. (1995) Fatty acid oxidation abnormalities in childhood-onset spinal muscular atrophy: primary or secondary defect(s)?. *Pediatr. Neurol.*, **12**, 21–30.

29. Crawford, T.O., Sladky, J.T. and Hurko, O. (1999) Abnormal fatty acid metabolism in childhood spinal muscular atrophy. *Ann. Neurol.*, **45**, 337–343.

30. Delves, P.J. and Roitt, I.M. (2000) The immune system. First of two parts. *N. Engl. J. Med.*, **343**, 37–49.

31. Delves, P.J. and Roitt, I.M. (2000) The immune system. Second of two parts. *N. Engl. J. Med.*, **343**, 108–117.

32. Mebius, R.E. and Kraal, G. (2005) Structure and function of the spleen. *Nat. Rev. Immunol.*, **5**, 606–616.

33. Tarantino, G., Scalera, A. and Finelli, C. (2013) Liver-spleen axis: intersection between immunity, infections and metabolism. *World J. Gastroenterol.*, **19**, 3534–3542.

34. Dachs, E., Hereu, M., Piedrafita, L., Casanovas, A., Calderó, J. and Esquerda, J.E. (2011) Defective neuromuscular junction organization and postnatal myogenesis in mice with severe spinal muscular atrophy. *J. Neuropathol. Exp. Neurol.*, **70**, 444–461.

35. Monani, U.R., Sendtner, M., Coovert, D.D., Parsons, D.W., Andreassi, C., Le, T.T., Jablonka, S., Schrank, B., Rossoll, W., Rossol, W., *et al.* (2000) The human centromeric survival

motor neuron gene (SMN2) rescues embryonic lethality in Smn(-/-) mice and results in a mouse with spinal muscular atrophy. *Hum. Mol. Genet.*, **9**, 333–339.

36. Eshraghi, M., McFall, E., Gibeault, S. and Kothary, R. (2016) Effect of genetic background on the phenotype of the Smn2B/- mouse model of spinal muscular atrophy. *Hum. Mol. Genet.*, Epub ahead of print.

37. Cesta, M.F. (2006) Normal structure, function, and histology of the spleen. *Toxicol. Pathol.*, **34**, 455–465.

38. Vacchio, M.S., Ciucci, T. and Bosselut, R. (2016) 200 Million Thymocytes and I: A Beginner's Survival Guide to T Cell Development. *Methods Mol Biol*, **1323**, 3–21.

39. Elmore, S.A. (2006) Enhanced histopathology of the thymus. *Toxicol. Pathol.*, **34**, 656–665.

40. Starr, T.K., Jameson, S.C. and Hogquist, K.A. (2003) Positive and negative selection of T cells. *Ann. Rev. Immunol.*, **21**, 139–176.

41. Hogquist, K.A., Baldwin, T.A. and Jameson, S.C. (2005) Central tolerance: learning self-control in the thymus. *Nat. Rev. Immunol.*, **5**, 772–782.

42. Lee, J.Y. and Love, P.E. (2016) Assessment of T Cell Development by Flow Cytometry. *Methods Mol Biol*, **1323**, 47–64.

43. Hu, Q., Nicol, S.A., Suen, A.Y. and Baldwin, T.A. (2012) Examination of thymic positive and negative selection by flow cytometry. *J. Vis. Exp.*, **68**, 4269.

44. Burlet, P., Huber, C., Bertrandy, S., Ludosky, M.A., Zwaenepoel, I., Clermont, O., Roume, J., Delezoide, A.L., Cartaud, J., Munnich, A., *et al.* (1998) The distribution of SMN protein complex in human fetal tissues and its alteration in spinal muscular atrophy. *Hum. Mol. Genet.*, **7**, 1927–1933.

45. Ransohoff, R.M. (2016) How neuroinflammation contributes to neurodegeneration. *Science*, **353**, 777–783.

46. Banerjee, R., Mosley, R.L., Reynolds, A.D., Dhar, A., Jackson-Lewis, V., Gordon, P.H., Przedborski, S. and Gendelman, H.E. (2008) Adaptive immune neuroprotection in G93A-SOD1 amyotrophic lateral sclerosis mice. *PloS One*, **3**,

47. O'Rourke, J.G., Bogdanik, L., Yáñez, A., Lall, D., Wolf, A.J., Muhammad, A.K., Ho, R., Carmona, S., Vit, J.P., Zarrow, J., *et al.* (2016) C9orf72 is required for proper macrophage and microglial function in mice. *Science*, **351**, 1324–1329.

48. Beers, D.R., Henkel, J.S., Zhao, W., Wang, J. and Appel, S.H. (2008) CD4+ T cells support glial neuroprotection, slow disease progression, and modify glial morphology in an animal model of inherited ALS. *Proc. Natl. Acad. Sci.*, **105**, 15558–15563.

49. Chiu, I.M., Chen, A., Zheng, Y., Kosaras, B., Tsiftsoglou, S.A., Vartanian, T.K., Brown, R.H., Jr. and Carroll, M.C. (2008) T lymphocytes potentiate endogenous neuroprotective inflammation in a mouse model of ALS. *Proc. Natl. Acad. Sci.*, **105**, 17913–17918.

50. Hirahara, H., Ogawa, M., Kimura, M., Iiai, T., Tsuchida, M., Hanawa, H., Watanabe, H. and Abo, T. (1994) Glucocorticoid independence of acute thymic involution induced by lymphotoxin and estrogen. *Cell. Immunol.*, **153**, 401–411.

51. Screpanti, I., Morrone, S., Meco, D., Santoni, A., Gulino, A., Paolini, R., Crisanti, A., Mathieson, B.J. and Frati, L. (1989) Steroid sensitivity of thymocyte subpopulations during intrathymic differentiation. Effects of 17 beta-estradiol and dexamethasone on subsets expressing T cell antigen receptor or IL-2 receptor. *J. Immunol.*, **142**, 3378–3383.

52. Savino, W. and Dardenne, M. (2000) Neuroendocrine control of thymus physiology. *Endocr. Rev.*, **21**, 412–443.

53. Hachiya, Y., Arai, H., Hayashi, M., Kumada, S., Furushima, W., Ohtsuka, E., Ito, Y., Uchiyama, A. and Kurata, K. (2005) Autonomic dysfunction in cases of spinal muscular atrophy type 1 with long survival. *Brain Dev.*, **27**, 574–578.

54. Araujo, A., Araujo, M. and Swoboda, K.J. (2009) Vascular perfusion abnormalities in infants with spinal muscular atrophy. *J. Pediatr.*, **155**, 292–294.

55. Rudnik, -Schöneborn, S. and Vogelgesang, S. (2010) Digital necroses and vascular thrombosis in severe spinal muscular atrophy. *Muscle Nerve*, **42**, 144–147.

56. Ackerman, K.D., Felten, S.Y., Dijkstra, C.D., Livnat, S. and Felten, D.L. (1989) Parallel development of noradrenergic innervation and cellular compartmentation in the rat spleen. *Exp. Neurol.*, **103**, 239–255.

57. Bellinger, D.L., Lorton, D., Felten, S.Y. and Felten, D.L. (1992) Innervation of lymphoid organs and implications in development, aging, and autoimmunity. *Int. J. Immunopharmacol.*, **14**, 329–344.

58. Baggiolini, M. (1998) Chemokines and leukocyte traffic. *Nature*, **392**, 565–568.

59. Rennert, P.D., Browning, J.L. and Mebius, R. (1996) Surface lymphotoxin alpha/beta complex is required for the development of peripheral lymphoid organs. *J. Exp. Med.*, **184**, 1999–2006.

60. Matsumoto, M., Fu, Y.X., Molina, H. and Chaplin, D.D. (1997) Lymphotoxin-alpha-deficient and TNF receptor-I-deficient mice define developmental and functional characteristics of germinal centers. *Immunol. Rev.*, **156**, 137–144.

61. Fütterer, A., Mink, K., Luz, A., Kosco-Vilbois, M.H. and Pfeffer, K. (1998) The lymphotoxin beta receptor controls organogenesis and affinity maturation in peripheral lymphoid tissues. *Immunity*, **9**, 59–70.

62. Förster, R., Schubel, A., Breitfeld, D., Kremmer, E., Renner-Müller, I., Wolf, E. and Lipp, M. (1999) CCR7 coordinates the primary immune response by establishing functional microenvironments in secondary lymphoid organs. *Cell*, **99**, 23–33.

63. Ettinger, R., Browning, J.L., Michie, S.A., van Ewijk, W. and McDevitt, H.O. (1996) Disrupted splenic architecture, but normal lymph node development in mice expressing a soluble lymphotoxin-beta receptor-IgG1 fusion protein. *Proc. Natl. Acad. Sci.*, **93**, 13102–13107.

64. Ngo, V.N., Korner, H., Gunn, M.D., Schmidt, K.N., Riminton, D.S., Cooper, M.D., Browning, J.L., Sedgwick, J.D. and Cyster, J.G. (1999) Lymphotoxin alpha/beta and tumor necrosis factor are required for stromal cell expression of homing chemokines in B and T cell areas of the spleen. *J. Exp. Med.*, **189**, 403–412.

65. Gunn, M.D., Kyuwa, S., Tam, C., Kakiuchi, T., Matsuzawa, A., Williams, L.T. and Nakano, H. (1999) Mice lacking expression of secondary lymphoid organ chemokine have defects in lymphocyte homing and dendritic cell localization. *J. Exp. Med.*, **189**, 451–460.

66. Geijtenbeek, T.B., Groot, P.C., Nolte, M.A., van Vliet, S.J., Gangaram-Panday, S.T., van Duijnhoven, G.C., Kraal, G., van Oosterhout, A.J. and van Kooyk, Y. (2002) Marginal zone macrophages express a murine homologue of DC-SIGN that captures blood-borne antigens in vivo. *Blood*, **100**, 2908–2916.

67. Koppel, E.A., Ludwig, I.S., Hernandez, M.S., Lowary, T.L., Gadikota, R.R., Tuzikov, A.B., Vandenbroucke-Grauls, C.M., van Kooyk, Y., Appelmelk, B.J. and Geijtenbeek, T.B. (2004) Identification of the mycobacterial carbohydrate structure that binds the C-type lectins DC-SIGN, L-SIGN and SIGNR1. *Immunobiology*, **209**, 117–127.

68. Elomaa, O., Kangas, M., Sahlberg, C., Tuukkanen, J., Sormunen, R., Liakka, A., Thesleff, I., Kraal, G. and Tryggvason, K. (1995) Cloning of a novel bacteria-binding receptor structurally related to scavenger receptors and expressed in a subset of macrophages. *Cell*, **80**, 603–609.

69. Jones, C., Virji, M. and Crocker, P.R. (2003) Recognition of sialylated meningococcal lipopolysaccharide by siglecs expressed on myeloid cells leads to enhanced bacterial uptake. *Mol. Microbiol.*, **49**, 1213–1225.

70. Narver, H.L., Kong, L., Burnett, B.G., Choe, D.W., Bosch-Marcé, M., Taye, A.A., Eckhaus, M.A. and Sumner, C.J. (2008) Sustained improvement of spinal muscular atrophy mice treated with trichostatin A plus nutrition. *Ann. Neurol.*, **64**, 465–470.

71. Tsai, L.K.K., Tsai, M.S.S., Lin, T.B.B., Hwu, W.L.L. and Li, H. (2006) Establishing a standardized therapeutic testing protocol for spinal muscular atrophy. *Neurobiol. Dis.*, **24**, 286–295.

72. Hsieh-Li, H., Chang, J.G., Jong, Y.J., Wu, M.H., Wang, N.M., Tsai, C. and Li, H. (2000) A mouse model for spinal muscular atrophy. *Nat. Genet.*, **24**, 66–70.

73. Somers, E., Lees, R.D., Hoban, K., Sleigh, J.N., Zhou, H., Muntoni, F., Talbot, K., Gillingwater, T.H. and Parson, S.H. (2016) Vascular Defects and Spinal Cord Hypoxia in Spinal Muscular Atrophy. *Ann. Neurol.*, **79**, 217–230.

74. Somers, E., Stencel, Z., Wishart, T.M., Gillingwater, T.H. and Parson, S.H. (2012) Density, calibre and ramification of muscle capillaries are altered in a mouse model of severe spinal muscular atrophy. *Neuromuscul. Disord.*, **22**, 435–442.

75. Turner, M.D., Nedjai, B., Hurst, T. and Pennington, D.J. (2014) Cytokines and chemokines: At the crossroads of cell signalling and inflammatory disease. *Biochim. Biophys. Acta*, **1843**, 2563–2582.

76. Shafey, D., Boyer, J.G., Bhanot, K. and Kothary, R. (2010) Identification of novel interacting protein partners of SMN using tandem affinity purification. *J. Proteome Res.*, **9**, 1659–1669.